

H₂O and CO₂ Surface Contamination of the Lithium-Stuffed Garnet

Yuheng Li,[†] Asmee M. Prabhu,[‡] Tej S. Choksi,^{*,‡} and Pieremanuele Canepa^{*,†,¶}

[†]*Department of Materials Science and Engineering, National University of Singapore, 9
Engineering Drive 1, 117575, Singapore*

[‡]*School of Chemical and Biomedical Engineering, Nanyang Technological University,
Singapore 637459, Singapore*

[¶]*Department of Chemical and Biomolecular Engineering, National University of Singapore,
4 Engineering Drive 4, 117585, Singapore*

E-mail: tej.choksi@ntu.edu.sg; pcanepa@nus.edu.sg

Abstract

Understanding the reactivity of ubiquitous molecules on complex oxides has broad impacts in energy applications and catalysis. The garnet-type Li₇La₃Zr₂O₁₂ is a promising solid-state electrolyte for lithium(Li)-ion batteries, and it readily reacts with H₂O and CO₂ when exposed to ambient air. Such reactions form a contamination layer on Li₇La₃Zr₂O₁₂ that is detrimental to the battery operations. The strong interactions of Li₇La₃Zr₂O₁₂ with H₂O and CO₂, however, make Li₇La₃Zr₂O₁₂ a promising support to catalyze H₂O dissociation and CO₂ adsorption. Here, using first-principles calculations, we investigate the adsorption and reactions of H₂O and CO₂ on a Li₇La₃Zr₂O₁₂ surface. We show that H₂O reacts through the exchange of proton and Li⁺ and produces metal hydroxide species. At high H₂O coverage, half of the H₂O molecules dissociate while the other half remain intact. CO₂ reacts with the Li₇La₃Zr₂O₁₂ surface directly to produce carbonate species. We clarify that the individual reactions of H₂O and CO₂ with

$\text{Li}_7\text{La}_3\text{Zr}_2\text{O}_{12}$ are more thermodynamically favorable than the co-adsorption of H_2O and CO_2 . Finally, we demonstrate that low temperature and high partial pressure promote the reactions of H_2O and CO_2 with $\text{Li}_7\text{La}_3\text{Zr}_2\text{O}_{12}$. For energy storage application of $\text{Li}_7\text{La}_3\text{Zr}_2\text{O}_{12}$, our study guides processing conditions to minimize surface contamination. From a catalysis point of view, our findings reveal the potential of using complex oxides, such as $\text{Li}_7\text{La}_3\text{Zr}_2\text{O}_{12}$ as a support for reactions requiring H_2O dissociation and strong CO_2 adsorption.

1 Introduction

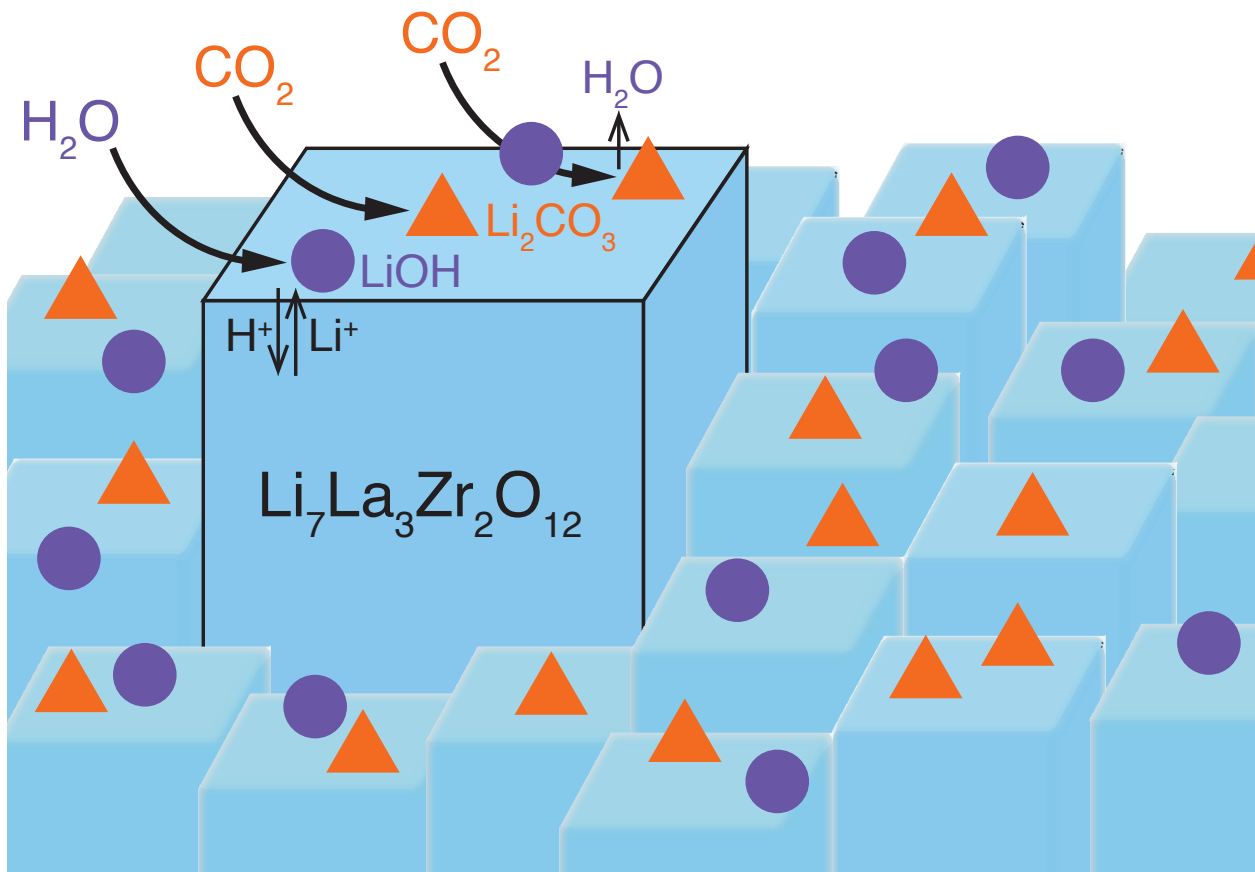
Energy storage and conversion devices relying on complex oxides are central to the decarbonization of our planet.¹⁻⁴

On one hand, lithium(Li)-ion batteries based on oxide chemistries,^{1,5} offer an appealing strategy to store green-energy produced by photo-voltaic panels, wind turbines, hydropower and/or hydroelectric means. Li batteries suffer from safety issues, mostly due to the flammability of liquid electrolytes.¹ Solid-state batteries, replacing the flammable electrolyte with a solid “ceramic” —solid electrolytes— are safer alternatives.⁶⁻⁹ When suitably doped, the garnet-like quaternary oxide $\text{Li}_7\text{La}_3\text{Zr}_2\text{O}_{12}$ charts a solid electrolyte with unprecedented Li^+ conductivities ($\sim 10^{-6}$ – 10^{-3} S/cm).¹⁰⁻²⁴ Importantly, $\text{Li}_7\text{La}_3\text{Zr}_2\text{O}_{12}$ is claimed to be stable against high-energy density Li-metal anodes, which is an appealing feature for high-energy density batteries enabling vehicular transportation.^{20,22-25}

On the other hand, complex oxides catalyze the decomposition of abundant molecules, such as H_2O and CO_2 .²⁶⁻³⁰ Water dissociation during water-gas shift is a vital elementary step that is promoted by oxide supports, such as Al_2O_3 , CeO_2 , CuO , La_2O_3 , Mn_2O_4 , TiO_2 , Y_2O_3 , ZrO_2 , etc.³¹⁻³⁷ Complex oxides are extensively studied as catalytic supports to adsorb CO_2 from dilute gas streams and subsequently transform CO_2 into valuable chemicals production.^{36,38-43}

Here, using $\text{Li}_7\text{La}_3\text{Zr}_2\text{O}_{12}$ as an example, in the framework of *ab initio* thermodynamics we investigate the reactivity of this complex oxide with two ubiquitous molecules: H_2O and CO_2 . Previous work by Sharafi et al. using Raman and X-ray photo-emission spectroscopy (XPS) revealed the existence of thick layers (~ 5 – 10 nm) of Li_2CO_3 on the $\text{Li}_7\text{La}_3\text{Zr}_2\text{O}_{12}$ surfaces, upon exposure to air.^{21,23} The same authors also detected LiOH on the $\text{Li}_7\text{La}_3\text{Zr}_2\text{O}_{12}$ particles. The cartoon of Scheme 1 shows the bulk CO_2 and H_2O reactions with $\text{Li}_7\text{La}_3\text{Zr}_2\text{O}_{12}$ hypothesized by preliminary bulk reactions proposed by Sharafi et al.¹⁹ using density functional theory (DFT).

Nevertheless, the complexity of $\text{Li}_7\text{La}_3\text{Zr}_2\text{O}_{12}$ and other garnets in general, suggests that



Scheme 1: Possible reaction pathways for $\text{Li}_7\text{La}_3\text{Zr}_2\text{O}_{12}$ particle contamination when exposed to H_2O and CO_2 .

considering reactions of CO_2 and H_2O beyond the bulk structure is necessary.¹⁹ Specifically, if the structural heterogeneity of active sites on low index crystal planes contributes to activating closed shell species, such as CO_2 and H_2O . Here, we investigate this complex reactivity using DFT calculations of $\text{Li}_7\text{La}_3\text{Zr}_2\text{O}_{12}$ slabs interacting with H_2O and CO_2 . The computed surface phase-diagrams reveal that at room temperature and ambient pressures H_2O adsorbs vigorously on the exposed Li sites at the $\text{Li}_7\text{La}_3\text{Zr}_2\text{O}_{12}$ surfaces, nucleating LiOH and protons. These protons are then exchanged with the highly-mobile Li^+ -ions and

may "intercalate" in the $\text{Li}_7\text{La}_3\text{Zr}_2\text{O}_{12}$ bulk.¹⁴ Likewise, our simulations demonstrate that CO_2 adsorbs on the $\text{Li}_7\text{La}_3\text{Zr}_2\text{O}_{12}$ surfaces and readily transforms into carbonate species.

If $\text{Li}_7\text{La}_3\text{Zr}_2\text{O}_{12}$ is to be used in battery devices, our simulations provide guidelines to curb its degradation by CO_2 and H_2O . In contrast, spontaneous H_2O dissociation on $\text{Li}_7\text{La}_3\text{Zr}_2\text{O}_{12}$ makes it potentially relevant for the water-gas shift reaction,^{44,45} while the strong chemisorption of CO_2 makes $\text{Li}_7\text{La}_3\text{Zr}_2\text{O}_{12}$ a promising dual functional material for CO_2 capture and conversion.^{46,47} Hence, in the context of catalysis, $\text{Li}_7\text{La}_3\text{Zr}_2\text{O}_{12}$ appears an excellent catalyst support to investigate reactions of CO_2 activation and water splitting, respectively. These results are important to chart the reactivity of this complex quaternary oxide, which may be extended to other complex oxides.

2 Computational Methods

The chemical reactions at the surfaces of $\text{Li}_7\text{La}_3\text{Zr}_2\text{O}_{12}$ were probed with Kohn-Sham DFT simulations,⁴⁸ and approximated by the Perdew-Burke-Ernzerhof (PBE) functional.⁴⁹ Van der Waals (vdW) interactions were treated with the D3 method with a Becke-Johnson (BJ) damping term.^{50–52} The wavefunctions were expanded as plane-waves and core electrons by the projector-augmented wave (PAW) method as in VASP.^{53–56} The PAW potentials and the recommended cutoffs energies were: C 08Apr2002 400 eV, H 15Jun2001 250 eV, La 06Sep2000 219 eV; Li_sv 23Jan2001 272 eV; O 08Apr2002 400 eV; and Zr_sv 07Sep2000 230 eV. Slab optimizations were performed in two steps: *i*) a preliminary PBE and Γ -point optimization, and *ii*) optimization with PBE+D3-BJ with a $2\times 2\times 1$ k -mesh and a cutoff energy of 440 eV. The total energy was converged to 1×10^{-5} eV/cell and forces acting on atoms to within 0.01 eV/Å. We concluded with a final single-point energy calculations at a higher cut-off of 520 eV and integrated over a $4\times 4\times 1$ k -point grid.

As in this study we probe the adsorption and reactivity of molecules at the surface of $\text{Li}_7\text{La}_3\text{Zr}_2\text{O}_{12}$, it is crucial to treat explicitly the effect of vdW forces. vdW interactions were

captured by the D3+BJ method.^{50–52} Using these settings, the lattice constants ($a = 13.085 \text{ \AA}$ and $c = 12.579 \text{ \AA}$) of the tetragonal ($Ia4_1/acd$) $\text{Li}_7\text{La}_3\text{Zr}_2\text{O}_{12}$ were used to rescale the (010) slab models from Ref. 24. The (010) Li-terminated off-stoichiometric $\text{Li}_7\text{La}_3\text{Zr}_2\text{O}_{12}$ model contains 248 atoms, and has a surface energy of $\sim 1.34 \text{ J/m}^2$. The dispersion corrections (D3-BJ) increase the stability of the bulk structure, resulting in an increased surface energy by $\sim 0.50 \text{ J/m}^2$ compared to Ref. 24. A well-converged vacuum size of 15 \AA was used to eliminate spurious slab-slab (and adsorbate-adsorbate) interactions along the direction orthogonal to the surface plane.

A bulk-like region of the slab where all atomic positions are fixed was introduced in the middle of the slab models. A 40% bulk-like region was determined from convergence tests on slab total energies (see Figure S1 in Supporting Information) at which the total energy is converged to $\sim 7 \text{ meV}$ and relatively modest computational costs. Note, this procedure is commonly applied in surface science and catalysis to reduce significantly the computer time of structure optimization of large slab models.⁵⁷ Benchmark tests on $\text{Li}_7\text{La}_3\text{Zr}_2\text{O}_{12}$ bulk lattice constants and surface energies were performed to compare the effects of DFT functionals, i.e., PBE, PBE+D3 without damping, and PBE+D3 with BJ damping (see Table S1 of SI).

The coordination numbers and Mulliken charges were derived from the crystal orbital Hamilton populations (COHP) available in the Lobster code.⁵⁸ For the COHP calculations, the energy range is set to $-15 \sim 10 \text{ eV}$, and basis functions same as those in the PAW potentials are used for projections.

The adsorption energy (ΔE_{ads}) was calculated using Eq. 1:⁵⁹

$$\Delta E_{\text{ads}} = \frac{1}{2n} [E(\text{slab}|2n\text{H}_2\text{O}^{\text{ads}}) - E(\text{slab}) - 2nE(\text{H}_2\text{O}^{\text{g}})], \quad (1)$$

where $n = 1$ is the number of adsorbed molecules on each side of the slab model. In Eq. 1 we approximated the Gibbs energy of each term by the DFT total energy (i.e., $G \approx E$), thus neglecting the zero point energy, the pV and entropy contributions. $E(\text{slab}|2n\text{H}_2\text{O}^{\text{ads}})$ is the

total energy for the slab adsorbed with $n\text{H}_2\text{O}$ (on each surface side), $E(\text{slab})$ is total energy for the clean-surface slab, and $E(\text{H}_2\text{O}^g)$ is total energy for H_2O in gas phase. From Eq. 1, a more negative ΔE_{ads} value indicates a more favorable interaction of the adsorbate with the surface.

The energy changes computed as function of H_2O (and CO_2) coverage are calculated in terms of the Landau grand-potential energy, Ω of Eq. 2.

$$\begin{aligned}\Omega(x/5 \text{ ML}) &= \frac{1}{2A} [G(\text{slab}|2x\text{H}_2\text{O}^{\text{ads}}) - (12 - 2x)\mu^{T,P}(\text{H}_2\text{O}^g)], \\ &\approx \frac{1}{2A} [E(\text{slab}|2x\text{H}_2\text{O}^{\text{ads}}) - 2xTS_{\text{vib}}^T(\text{H}_2\text{O}^{\text{ads}}) - (12 - 2x)\mu^{T,P}(\text{H}_2\text{O}^g)],\end{aligned}\quad (2)$$

where x is the number of sites adsorbed on each surface, A is the surface area, and T and P are temperature and partial pressure of H_2O , respectively. $G(\text{slab}|2x\text{H}_2\text{O}^{\text{ads}})$ is the Gibbs free energy of the adsorbed slab and approximated as in Eq. 3, by $E(\text{slab}|2x\text{H}_2\text{O}^{\text{ads}})$ the DFT total energy of the slab adsorbing $x\text{H}_2\text{O}$ molecules on each surface. $S_{\text{vib}}^T(\text{H}_2\text{O}^{\text{ads}})$ is the vibrational entropy of the adsorbed H_2O (in either dissociated or intact form), calculated by fixing all atoms except the adsorbate. $\mu^{T,P}(\text{H}_2\text{O}^g)$ is the chemical potential of H_2O gas approximated by its DFT total energy in vacuum, corrected by the zero-point energy, and scaled to a given T and P condition using the Shomate equation.⁶⁰ Then, the change of grand-potential energy $\Delta\Omega$ ($x/5 \text{ ML}$) at different water coverage is computed in Eq. 4 with respect to the clean surface ($0/5 \text{ ML}$).

$$\Delta\Omega(x/5 \text{ ML}) = \Omega(x/5 \text{ ML}) - \Omega(0/5 \text{ ML}). \quad (4)$$

3 Results

3.1 $\text{Li}_7\text{La}_3\text{Zr}_2\text{O}_{12}$ (010) Surface and Selection of Adsorption Sites

Our analysis begins by selecting the energetically most favorable surface cut of $\text{Li}_7\text{La}_3\text{Zr}_2\text{O}_{12}$ from Ref. 24. The off-stoichiometry Li-terminated (010) surface (and identical to the (100) and the (001) surfaces) displays the lowest surface energy ($\sim 0.87 \pm 0.02$ J/m²) and remains stable even at high temperatures (~ 1000 K), targeted by typical thermal treatments of these oxides. The (010) surface corresponds to the dominant surface in the computed Wulff shapes of $\text{Li}_7\text{La}_3\text{Zr}_2\text{O}_{12}$, and it is representative of the real $\text{Li}_7\text{La}_3\text{Zr}_2\text{O}_{12}$ particles, either in sintered powders or sheet composites. Here, off-stoichiometric surfaces refer to surfaces where the stoichiometry deviates in composition from the bulk. As described in the Computational Methods (Section 2), the (010) surface from Ref. 24 was rescaled and recalculated in this study with the incorporation of vdW interactions.

When studying the adsorption of molecules on surfaces, a non-negligible challenge is selecting chemically sound adsorption configurations from the sheer number of imaginable adsorption conformations. This is especially true in complex oxides, such as $\text{Li}_7\text{La}_3\text{Zr}_2\text{O}_{12}$ which contains three chemically distinct cations with varying local coordination environments of oxygen atoms. We used pymatgen to ease the identification of unique adsorption sites, and subsequently construct initial structure of adsorbates bound to these sites.⁶¹ To prevent well-known convergence problems of slab calculations in the presence of fictitious electrical dipoles from polar adsorbates (H_2O here), we adsorbed molecules on both surface sides.⁶²

Tasked to clarify the mechanisms of H_2O and CO_2 reactions with $\text{Li}_7\text{La}_3\text{Zr}_2\text{O}_{12}$, it is first necessary to create appropriate adsorption models by understanding the characteristics of different active sites on this structurally heterogeneous surface. These characteristics include the proximity of active sites to the $\text{Li}_7\text{La}_3\text{Zr}_2\text{O}_{12}$ surface, their local environment, their Mulliken charges, and their coordination numbers.

Figure 1(a) and (b) show side and top views of the off-stoichiometric Li-terminated (010)

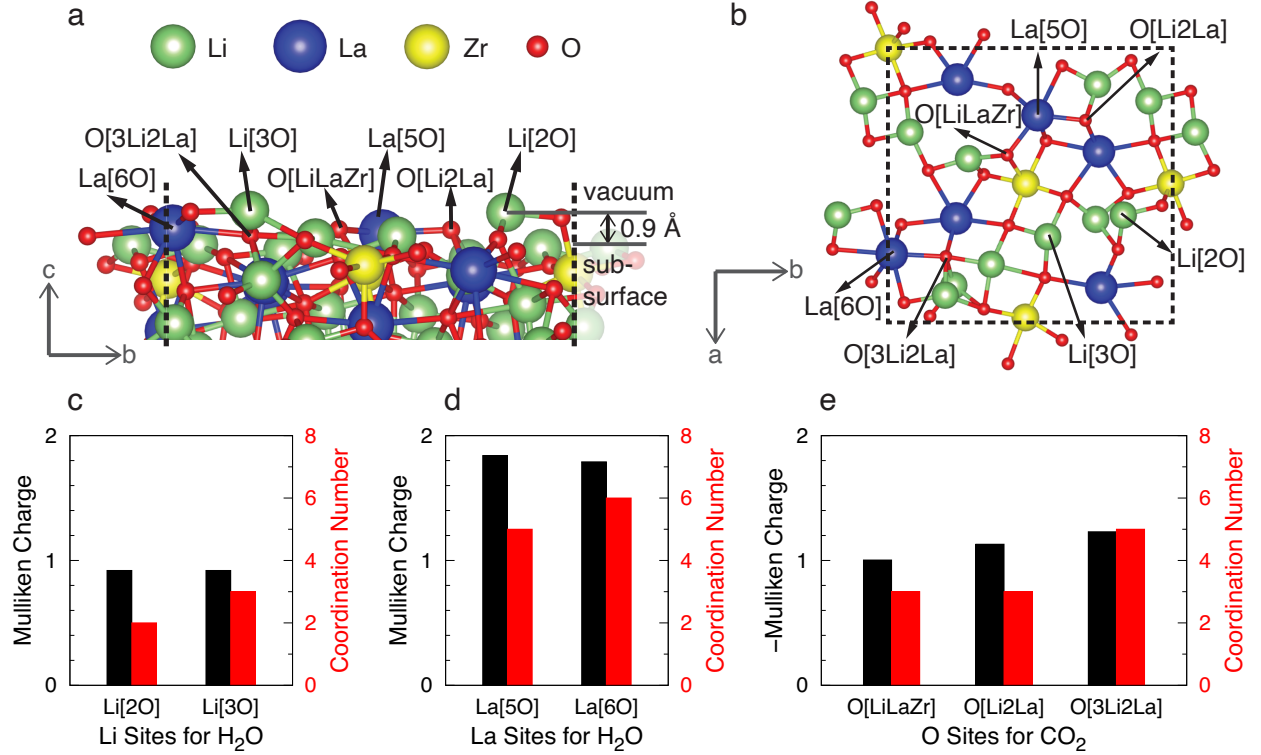


Figure 1: Properties of the adsorption sites on a $\text{Li}_7\text{La}_3\text{Zr}_2\text{O}_{12}$ surface. (a) Side view and (b) top view of the off-stoichiometry Li-terminated (010) surface of $\text{Li}_7\text{La}_3\text{Zr}_2\text{O}_{12}$. The boundary of the slab unit cell is marked with dashed lines. Li, La, Zr, and O species are shown in green, blue, yellow, and red, respectively. The surface adsorption sites are identified within $\sim 0.9 \text{ \AA}$ vertical range (panel (a)). The double headed arrow marks the surface range, outside of which are the vacuum and subsurface. Sites are denoted by the element followed by ions immediately bonded to the site. The 7 unique sites are: 2 types of Li (Li[3O] and Li[2O]), 2 types of La (La[6O] and La[5O]), 3 types of O (O[3Li2La], O[Li2La], and O[LiLaZr]), respectively. For a clearer view of sites' local environments, we concealed atoms far away from the surface. Mulliken charges (black bars) and coordination numbers (red bars) for Li sites in (c), La sites in (d), and O sites in (e). Li and La sites show positive Mulliken charges, indicating their electro-positive character, and *vice versa* for O sites.

surface of $\text{Li}_7\text{La}_3\text{Zr}_2\text{O}_{12}$. By defining a range of search, along the non-periodic direction of the slab of $\sim 0.9 \text{ \AA}$ from the most exposed atom at the surface, we identified 10 on-top surface adsorption sites. These sites show different proximity to surface; we denote each site according to its element followed by all species bonded to it. Thus, in Figure 1 seven unique sites out of 10 were identified: two types of Li sites Li[2O] and Li[3O]; two types of

La sites La[5O] and La[6O]; and three types of O sites O[LiLaZr], O[Li2La], and O[3Li2La], respectively.

Nominally, positively charged ions, such as, Li^+ and La^{3+} at the $\text{Li}_7\text{La}_3\text{Zr}_2\text{O}_{12}$ surface will attract negatively polarized parts of the adsorbing molecules and *vice versa*.

Figures 1(c-e) show the computed Mulliken charges and coordination numbers for all seven types of adsorption sites. The Mulliken analysis is an intuitive (but not unique) way of repartitioning the electron charge density on each atom (and orbital) by projecting it onto individual orthonormalized atomic orbitals.⁶³ The surface sites of each species show similar Mulliken charges, albeit distinct coordination numbers. As expected, Li and La metal sites show positive Mulliken charges. From an adsorption point of view, these sites will behave as Lewis acids in favor of accepting electrons from the oxygen lone-pair of H_2O . Indeed, the reactivity of these cations follows the scale of absolute hardness, η : Li^+ (~ 35.1 eV) $>$ La^{3+} (~ 15.4 eV) \gg Zr^{3+} (~ 5.68 eV),^{64,65} with Li^+ the most electrophilic cation of the three. Since Zr^{3+} is the least reactive metal of the three, we will not consider its reactivity in the remainder of this study. Oxygen sites reveals their basic character, and potentially driving the CO_2 adsorption via the C atom. We use this knowledge to guide our understanding of the adsorption and dissociation of H_2O and CO_2 on $\text{Li}_7\text{La}_3\text{Zr}_2\text{O}_{12}$.

3.2 H_2O Adsorption and Hydroxide Formation on $\text{Li}_7\text{La}_3\text{Zr}_2\text{O}_{12}$

Here, we provide the mechanistic insights of H_2O adsorption and reaction on the $\text{Li}_7\text{La}_3\text{Zr}_2\text{O}_{12}$ (010) surface to form hydroxide species.

Initially, we investigated the adsorption of a single H_2O molecule on the Li-terminated $\text{Li}_7\text{La}_3\text{Zr}_2\text{O}_{12}$ (010) surface. This low coverage analysis enables us to probe the surface characteristics of the surface. For every Li or La site, one H_2O was adsorbed on each side of the slab model, which eliminates any potential electrical dipoles caused by polar H_2O .⁶² The adsorption energies (ΔE_{ads}) of Eq. 1 were computed for all five Li and La sites of Figure 1.⁵⁹

Notably, the calculated ΔE_{ads} indicate high propensity of a H_2O molecule toward Li^+

sites ($\Delta E_{\text{ads}} = -1.21$ eV) compared to La^{3+} sites (-0.85 eV), clearly following the scale of cation absolute hardness by Parr and Pearson, with Li^+ (~ 35.1 eV) $>$ La^{3+} (~ 15.4 eV).

Figure 2 shows the diagram of the computed adsorption energies and a magnification of the adsorption sites for the two most favorable adsorption cases, which always occur on exposed Li sites.

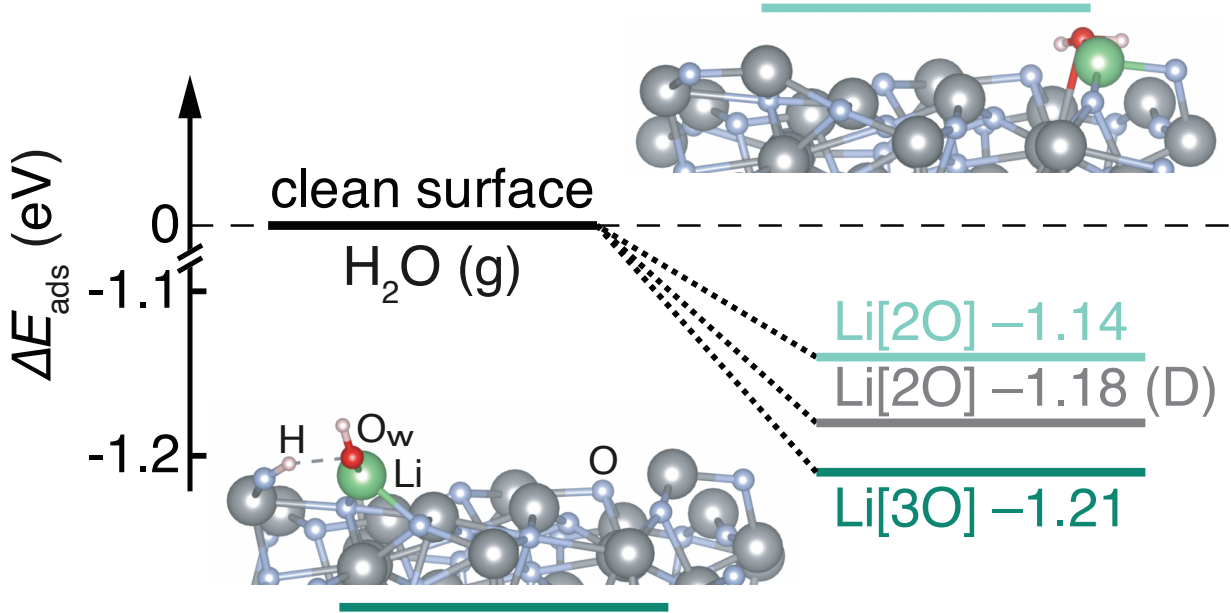


Figure 2: Adsorption energy for H_2O on the two most favorable sites Li[2O] (light green) and Li[3O] (dark green) on the Li-terminated $\text{Li}_7\text{La}_3\text{Zr}_2\text{O}_{12}$ (010) surface. The H_2O molecule on Li[2O] remains intact after adsorption (upper inset), while H_2O on Li[3O] dissociates to form LiOH (lower inset). The grey Li[2O] level marked with a “(D)” shows adsorption energy for a model where we forced H_2O dissociation on the Li[2O] site. Atomic species not directly involved in the adsorption are greyed out.

For the most favorable Li[3O] site (dark green line), H_2O dissociates accompanied by a significant ΔE_{ads} (~ -1.21 eV), and reacts with the Li site to form LiOH (see lower inset of Figure 2). Upon H_2O dissociation, a OH^- group is formed between the proton released and an adjacent oxygen atom of the surface; the OH^- group forms hydrogen bond with the O of the LiOH formed on the Li[3O] site. In the 2nd most favorable Li[2O] site (see upper inset of Figure 2), the adsorbed H_2O remains intact, yielding still a non-negligible ΔE_{ads} of

~ -1.14 eV, but comparatively less favorable than the Li[3O] site by ~ 70 meV. Notably, we attempted the dissociation of H_2O on the Li[2O] site with a calculated ΔE_{ads} of ~ -1.18 eV, indicating that the dissociation is thermodynamically favorable by ~ -40 meV with respect to non-dissociative adsorption at these sites.

It is important to unearth the causes behind the significant magnitudes of ΔE_{ads} and dissociation behaviors of H_2O on different metal sites. We observed that if the coordinates of the surface sub-layers and the inner region of the surface (making $\sim 80\%$ of the slab) are held frozen to that of the bulk slab, the adsorbed H_2O will not dissociate on any site, regardless of their chemical activities. Clearly, with such a constraint in place, the adsorption energy does not benefit from the reorganization of the surface atoms, which promotes the dissociative adsorption of H_2O . Thus, the adsorption energy follows the trend of the site exposure to the surface, with the top (bottom) site showing the most negative adsorption energy. In contrast, by constraining only 40% of the slab model, as in the rest of this study, the adsorbed H_2O on specific sites readily dissociates during the geometry optimization. Note that such preference for dissociation caused by rearrangements of atoms in the surface sub-layers is rarely seen in metals.

Unsurprisingly, H_2O dissociation lowers the adsorption energy. With a stabilizing contribution arising from H_2O dissociation, the adsorption energy no longer follows the trend of sites' proximity to the surface. From top to sub-layer sites in the surface, the adsorption energies are: -1.14 eV (Li[2O]), -1.21 eV (Li[3O]), -0.85 eV (La[5O]), -0.80 eV (La[6O]), and -0.65 eV (Li[3O]). Furthermore, our results clearly indicate that the dissociation behavior depends on local environment of the adsorption site. If a specific adsorption configuration displays oxygen atoms in the vicinity of the adsorption site, protons from adsorbed H_2O readily dissociate to bond with the surface oxygen species. The dissociative adsorption of H_2O is well understood in previous studies of metal oxides including rutile- TiO_2 , anatase- TiO_2 , and rutile- RuO_2 .^{66–68} In general, we find that adsorbed H_2O tends to dissociate when there are oxygen atoms within ~ 1.9 Å of the cation site (Table S2), unless there are metal

ions that can better stabilize H₂O adsorption via bonding with O in H₂O (see inset for Li[2O] in Figure 2). Therefore, values of ΔE_{ads} in Li₇La₃Zr₂O₁₂ are clearly affected by *i*) the site proximity to the surface and *ii*) H₂O dissociation driven by the local environment.

We are also interested in the bonding character of H₂O adsorption (or dissociation) on the Li₇La₃Zr₂O₁₂ surface since H₂O, a closed shell species, has significantly favorable ΔE_{ads} . First, we determined the dispersion contribution to the adsorption energy by comparing our predictions with (PBE-D3) and without Van der Waals’ contributions, hence just with GGA PBE.⁴⁹ The results show that there is a consistent dispersion contribution of only $\sim 15\text{--}20\%$ to the total DFT energies. This means that dispersion interactions are not a major source of bonding, and indicates a more dominant nature of chemisorption-driven reactions instead of physisorption.

Next, we compared changes of Mulliken charges of all Li, La sites and O of H₂O before and after H₂O adsorption (Figure S3(a, b) in SI). Unlike on reducible oxides (with open-shell *d* or *f* transition metals),^{69,70} there is no charge transfer between H₂O and the surface sites, which indicates the electrostatic nature of the interaction. These insights above agree with previous findings that intrinsic surface electrostatics in an insulating ionic system play a critical role in stabilizing the dangling lone pair of H₂O.⁷¹

Table 1: H₂O adsorption energy (in eV/molecule) at increasing number of molecules (ML). Site is the adsorption site. $\delta\Delta E_{\text{ads}}$ informs the change of ΔE_{ads} upon the addition of a H₂O molecule. The number of dissociated H₂O molecules (H₂O) are also indicated. LiOH indicates whether the addition of a new H₂O molecule promotes LiOH formation.

ML	Site	ΔE_{ads}	$\delta\Delta E_{\text{ads}}$	H ₂ O	LiOH
1/5	Li[3O]	-1.21	—	1	Yes
2/5	Li[2O]	-1.19	+0.02	1	No
3/5	La[5O]	-1.19	0.00	2	Yes
4/5	La[6O]	-1.10	+0.09	2	No
5/5	Li[3O]	-1.09	+0.01	3	Yes
6/5	Li[3O]	-1.07	+0.02	3	No

We now investigate the adsorption of multiple H₂O molecules to simulate reactions at high water coverage on the Li₇La₃Zr₂O₁₂ surface. All five Li and La sites were first ordered

according to their individual H_2O adsorption energy, from more negative to more positive. In particular, the order of adsorption energies is $\text{Li}[3\text{O}]$ (-1.21 eV) $<$ $\text{Li}[2\text{O}]$ (-1.14 eV) \ll $\text{La}[5\text{O}]$ (-0.85 eV) $<$ $\text{La}[6\text{O}]$ (-0.80 eV) $<$ $\text{Li}[3\text{O}]$ (-0.65 eV). Following this order of stability, we adsorbed H_2O on available metals sites achieving a complete H_2O monolayer (ML). For each additional molecule, the structure was relaxed before the next H_2O was adsorbed. After all five sites were adsorbed, we identified an additional Li site, which emerged from the surface re-organization upon the increasing water coverage. Eventually, six H_2O molecules were adsorbed on each side of the slab (12 in total).

Table 1 reports the ΔE_{ads} for H_2O on the (010) $\text{Li}_7\text{La}_3\text{Zr}_2\text{O}_{12}$ surface as the exposed metal site are progressively saturated. We denote the H_2O coverage as the fraction of one monolayer ($x/5$ ML). ΔE_{ads} for the same adsorptions but with all H_2O forced to dissociate is reported in Table S3.

Table 1 shows that the addition of subsequent H_2O molecules to the $\text{Li}_7\text{La}_3\text{Zr}_2\text{O}_{12}$ (010) surface from $1/5$ ML to $6/5$ ML gradually increase ΔE_{ads} to more positive values. This progressive increase is mainly caused by the more positive adsorption energy of each site, from -1.21 to -0.65 eV, dependent on their proximity to the surface and whether H_2O spontaneously dissociates. This increase is also likely due to additional H_2O – H_2O interactions as a result of crowding the $\text{Li}_7\text{La}_3\text{Zr}_2\text{O}_{12}$ surface, and the progressively neutralized and less reactive surface. Simultaneously, specific adsorption arrangements favor hydrogen bonding with the surface.

Figure 3(a) shows the energy diagram for all adsorption steps towards high H_2O coverage beyond one monolayer. $\Delta\Omega$ was calculated using Eq. 2–4 for increasing H_2O coverage at the partial pressure of 1 bar and at 300 K. A negative $\Delta\Omega$ means that H_2O adsorbs favorably on the $\text{Li}_7\text{La}_3\text{Zr}_2\text{O}_{12}$ surface. As more H_2O molecules adsorb, $\Delta\Omega$ continuously becomes more negative, indicating that the increasing coverage is favorable up to $6/5$ ML. This trend also suggests that H_2O can probably adsorb beyond $6/5$ ML. We also found a decreasing trend for the absolute difference of $\Delta\Omega$ between consecutive H_2O adsorptions. For example,

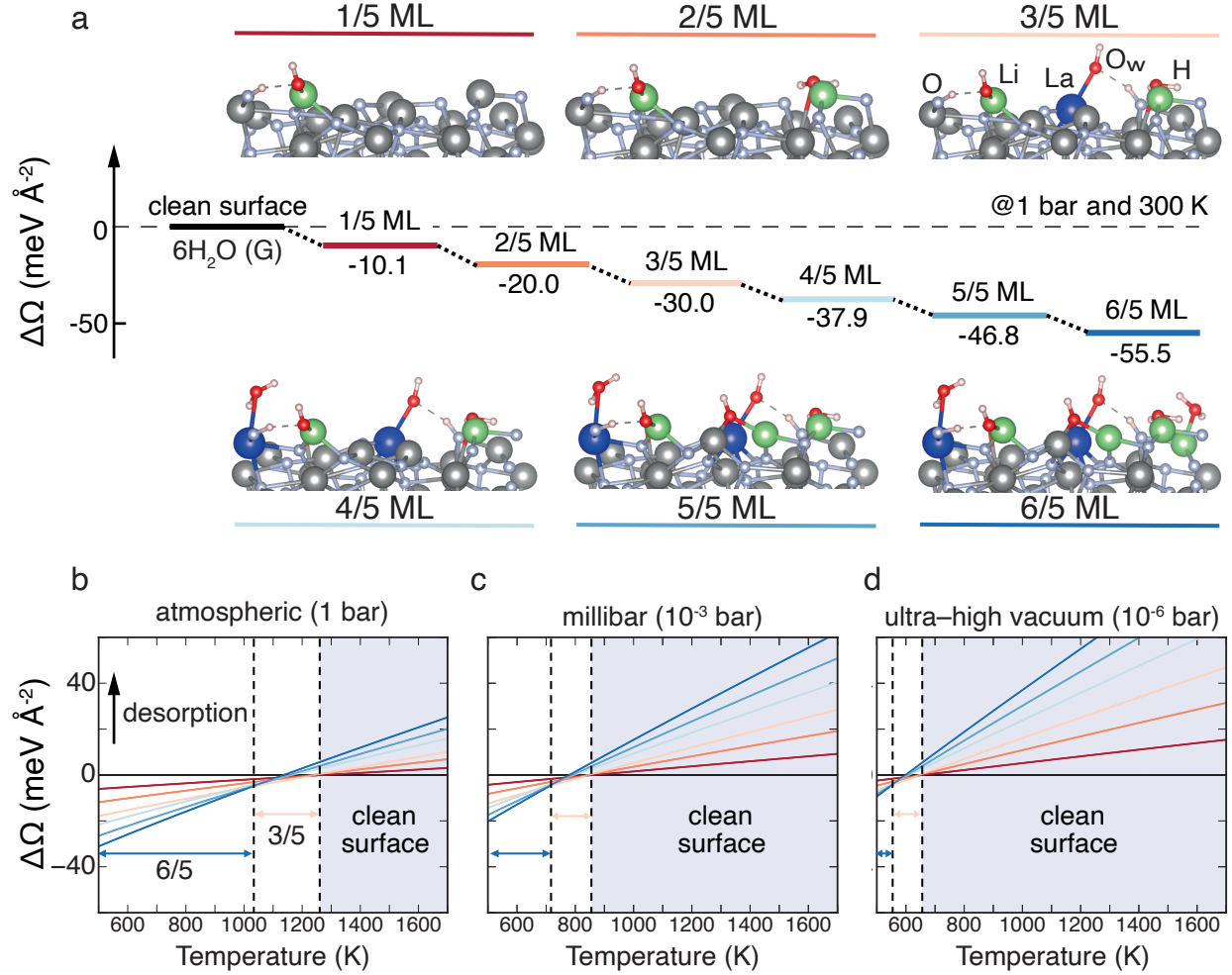


Figure 3: Change of grand-potential energy $\Delta\Omega$ relative to the clean $\text{Li}_7\text{La}_3\text{Zr}_2\text{O}_{12}$ surface and gas-phase H_2O at variable temperatures and pressures of technological relevance. In panel (a), the H_2O coverage is denoted by fraction of a monolayer (ML) of H_2O on the surface. Full coverage is achieved at 6/5 ML when all the five original sites plus an additional site are adsorbed. Increasing coverage is marked by divergent colors from red to blue. $\Delta\Omega$ as a function of temperature for different H_2O coverage and partial pressure of 1 (b, atmospheric regime), 1×10^{-3} (c, mbar regime), and 1×10^{-6} bar (d, ultra-high vacuum regime). Double arrows show the most favorable coverage within temperature ranges. Atomic species not directly involved in the adsorption are greyed out.

the absolute difference between $\Delta\Omega$ of 6/5 ML and 5/5 ML is $8.7 \text{ meV } \text{\AA}^{-2}$, less than $10.1 \text{ meV } \text{\AA}^{-2}$ between 1/5 ML and 0/5 ML. This decreasing difference is primarily attributed to the adsorption energy trends of individual sites, as less favored adsorption sites become occupied at higher coverages.

As we only consider adsorption sites within ~ 0.9 Å from the surface top (bottom), more adsorption sites may be available. Electrostatic repulsion between adsorbates should have only secondary effects on the increasingly more positive values of ΔE_{ads} . Furthermore, a progressive addition of H_2O molecules contributes to gradually neutralizing the highly reactive Li^+ sites. Indeed, at very high water coverage, beyond 6/5 ML, newly adsorbed H_2O molecules may not dissociate, even if dissociation is favored in a single H_2O adsorption on the same site.

For coverage up to 6/5 ML, half of the adsorbed H_2O molecules dissociate and react with surface to form LiOH (see Table 1). The same happens when all adsorbed H_2O molecules are forced to dissociate before relaxation (see Table S3). This “half-dissociation” trend was also observed for simple metal oxides like RuO_2 ,^{72,73} but a different water dissociation fraction of 75% was observed for the (101) surface in anatase- TiO_2 .⁷⁴ Note that the H_2O dissociation is spontaneous during geometry optimization, and thus it is not necessary to calculate their kinetic barriers explicitly (expected to be barrier-free). In terms of hydrogen bonding for adsorbates, the dissociated proton always forms hydrogen bonds with the oxygen atom in the original H_2O molecule. All H_2O adsorbates that remain intact form hydrogen bonds with adjacent surface O atoms.

Our analysis of the H_2O reactivity with the $\text{Li}_7\text{La}_3\text{Zr}_2\text{O}_{12}$ surfaces extends to conditions of technological relevance of this material. This analysis is relevant for the optimization of synthesis and heat treatment conditions in $\text{Li}_7\text{La}_3\text{Zr}_2\text{O}_{12}$ and common oxides. Figures 3(b, c, and d) show $\Delta\Omega$ as a function of temperature at atmospheric (1 bar), millibar (10^{-3} bar), and ultra-high vacuum (10^{-6} bar) partial pressures, respectively. The temperature range explored in Figures 3(b, c, and d) span those of typical synthesis and sintering temperature (~ 1000 °C) of $\text{Li}_7\text{La}_3\text{Zr}_2\text{O}_{12}$.¹⁶

At atmospheric conditions (Figure 3(b)), $\Delta\Omega$ at different coverage is plotted in the same color scheme as in Figure 3(a). A positive $\Delta\Omega$ indicates that adsorbed H_2O is in favor of desorption. We mark the most favorable coverage at different temperature ranges using

double headed arrows. In general, as the temperature increases, the H_2O coverage of the surfaces decreases until the surface of $\text{Li}_7\text{La}_3\text{Zr}_2\text{O}_{12}$ is water free. This situation is achieved for temperatures above ~ 1260 K (Figure 3 (b)). At lower temperatures (up to ~ 1030 K), the most favorable coverage is $6/5$ ML $\text{Li}_7\text{La}_3\text{Zr}_2\text{O}_{12}$, whereas the $3/5$ ML coverage is the most favorable condition in the temperature range 1030–1260 K. Considering even higher coverage, one would expect steeper lines than for $6/5$, resulting in water-rich surfaces of $\text{Li}_7\text{La}_3\text{Zr}_2\text{O}_{12}$. However, such conditions cannot change the scenario for higher temperature ranges (≥ 1260 K), exhibiting water-free $\text{Li}_7\text{La}_3\text{Zr}_2\text{O}_{12}$ surfaces.

Under millibar (Figure 3(c)) and ultra-high vacuum (Figure 3(d)) H_2O partial pressures, one can find the same general trends for coverage vs. temperature as under atmospheric pressure (Figure 3(a)). However, the temperature ranges setting a water-free clean surface of $\text{Li}_7\text{La}_3\text{Zr}_2\text{O}_{12}$ increases as H_2O partial pressure decreases. For example, in situations of ultra-high vacuum (Figure 3(d)), we predict an onset temperature of ~ 650 K at which the $\text{Li}_7\text{La}_3\text{Zr}_2\text{O}_{12}$ surfaces will be water-free. These findings indicate that low partial pressures are beneficial to minimize surface contamination with H_2O and LiOH .

3.3 CO_2 Adsorption and Carbonate Formation on $\text{Li}_7\text{La}_3\text{Zr}_2\text{O}_{12}$

We now focus on CO_2 adsorption on $\text{Li}_7\text{La}_3\text{Zr}_2\text{O}_{12}$ and its subsequent transformation into carbonate CO_3^{2-} species. We probed CO_2 adsorption on five oxygen sites of the Li-terminated $\text{Li}_7\text{La}_3\text{Zr}_2\text{O}_{12}$ surface, as shown in Figure 1. The adsorption is achieved by placing the carbon atom of CO_2 close (~ 1.17 Å) to the O site, to induce the formation of a C–O bond. The most favorable site is a O[LiLaZr], and its ΔE_{ads} is strikingly high ~ -2.21 eV —a clear indication of CO_2 chemisorption. The other sites show comparable (~ -1.65 – -1.31 eV) but more positive adsorption energies. The least favorable site is O[3Li2La], still with a sizeable ΔE_{ads} of ~ -1.31 eV.

Regardless of the binding oxygen site, the adsorbed CO_2 reorganize into carbonate CO_3^{2-} species after structure optimization. In detail, two oxygen atoms in CO_2 form bonds with

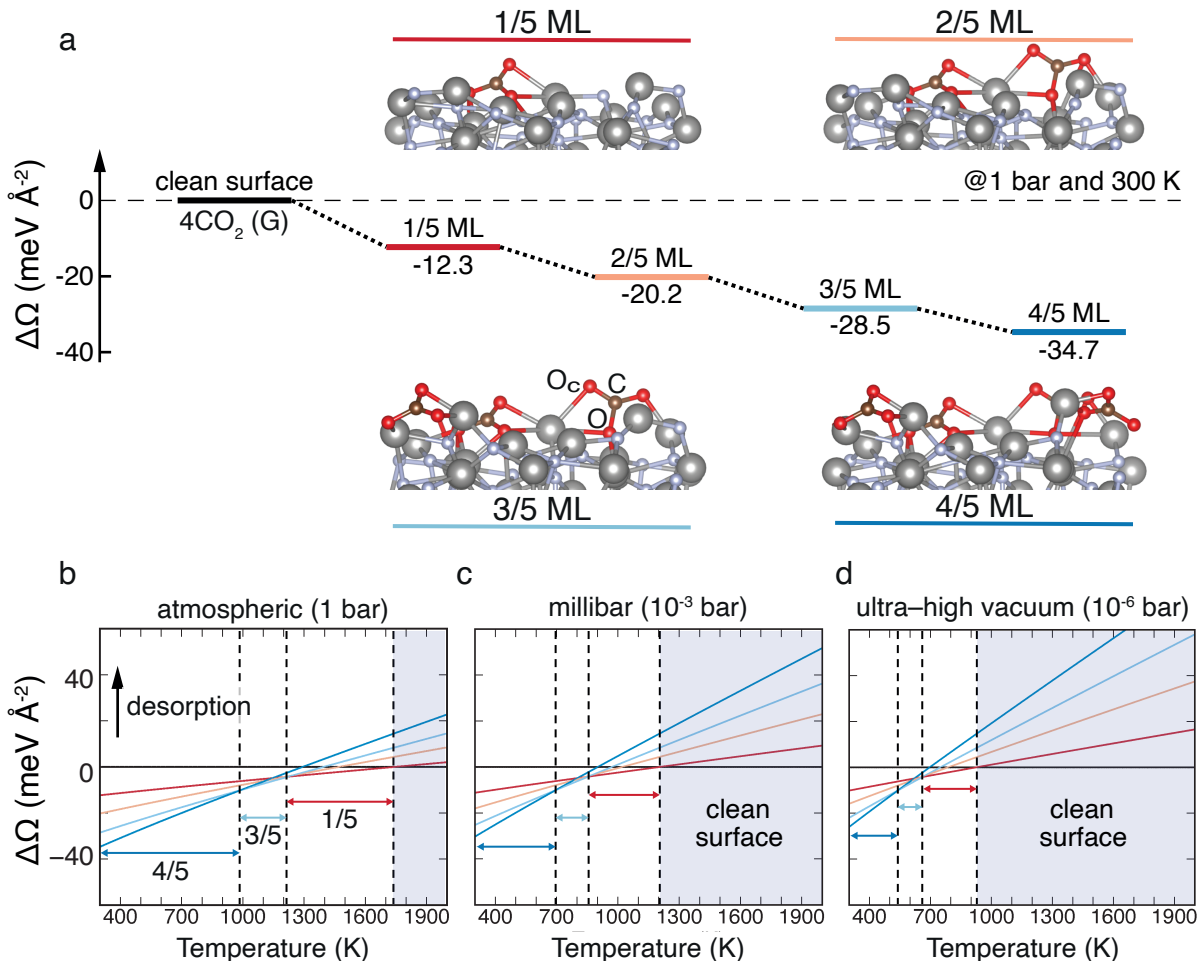


Figure 4: Change of grand potential $\Delta\Omega$ relative to clean surface and gas-phase CO_2 at variable temperatures and pressures of technological relevance. In panel (a), the CO_2 coverage is denoted by a fraction of CO_2 monolayer (ML) of the surface. $\Delta\Omega$ (in $\text{meV}/\text{\AA}^2$) as a function of temperature for different CO_2 coverage and partial pressure of 1 (b, atmospheric regime), 1×10^{-3} (c, millibar regime), and 1×10^{-6} bar (d, ultra-high vacuum regime), respectively. Double arrows denote the most favorable coverage within each temperature range. The structures and $\Delta\Omega$ for different coverage are marked using the same color scheme of four divergent colors. Atomic species not directly involved in the adsorption are greyed out.

metal ions available in the vicinity, with the carbonate species organizing in a polydentate conformation (Figure S1).⁷⁵ For all carbonates formed on the five sites, there are 13 bonds formed between surface metal ions and O of CO_2 , including eight Li-O bonds and five La-O bonds. The exceeding number of Li-O bonds show a clear preference for Li^+ over La^{3+}

ions. In particular, the surface carbonates show an average C–O bond length of ~ 1.31 Å, comparable to ~ 1.28 Å in bulk Li_2CO_3 .⁷⁶

The adsorption of CO_2 consists of two types of bonds: one between the carbon atom of CO_2 and a surface oxygen site, and the other between the oxygen atoms of CO_2 and metal ions of the surface. We observe that the incipient bond between O and metal-ion on $\text{Li}_7\text{La}_3\text{Zr}_2\text{O}_{12}$ has major contributions to the values of ΔE_{ads} . On different adsorption sites, the strength for the O and metal ion bonding depends on which metal ions are proximal to the site.

We also determined the bonding nature for CO_2 chemisorbed on $\text{Li}_7\text{La}_3\text{Zr}_2\text{O}_{12}$. Indeed, the dispersion contributions are calculated to be only $\sim 15\text{--}20\%$, similar to the cases of H_2O adsorption discussed earlier. Charge transfer is then analyzed through changes of Mulliken charges upon adsorption. Figure S3 shows that the average changes are ~ 0.30 for the surface O sites and ~ -0.26 for C in CO_2 . Besides, the average change upon adsorption is ~ -0.22 for O in CO_2 , ~ -0.01 for surface Li ions bonded to O, and ~ 0.12 for La ions. These changes are slightly larger than those for H_2O adsorption (~ -0.05 for Li sites, ~ 0.07 for La sites, and ~ 0.03 for O in H_2O , see Figure S3 in SI). Taken together, this analysis confirms that the structural heterogeneity of surface sites on $\text{Li}_7\text{La}_3\text{Zr}_2\text{O}_{12}$ (010) enables strong adsorption of H_2O and CO_2 , which are otherwise known to physisorb on metals and ionic oxides. While such robust adsorption events are detrimental for the application of $\text{Li}_7\text{La}_3\text{Zr}_2\text{O}_{12}$ in energy storage, they indicate that $\text{Li}_7\text{La}_3\text{Zr}_2\text{O}_{12}$ is a potentially interesting catalyst support for H_2O activation and adsorbing CO_2 from dilute streams.

We then studied CO_2 adsorption as a function of CO_2 coverage. CO_2 was sequentially adsorbed on all five O sites available on the $\text{Li}_7\text{La}_3\text{Zr}_2\text{O}_{12}$ surface. The sequential adsorption following the order of their individual adsorption energies, from more negative to more positive ($\text{O}[\text{LiLaZr}]$ (-2.21 eV) \ll $\text{O}[\text{Li2La}]$ (-1.65 eV) $<$ $\text{O}[\text{LiLaZr}]$ (-1.58 eV) $<$ $\text{O}[\text{LiLaZr}]$ (-1.34 eV) $<$ $\text{O}[\text{3Li2La}]$ (-1.31 eV)). In the process to adsorb the last CO_2 onto the $\text{Li}_7\text{La}_3\text{Zr}_2\text{O}_{12}$ surface, the $\text{O}[\text{3Li2La}]$ site was found unfavorable, as adsorbed CO_2 on this site was too close

(~ 1.20 Å) to a La^{3+} on the reconstructed surface. Eventually, there are only four out of five oxygen sites available for CO_2 adsorption, which set the highest CO_2 coverage to 4/5 ML. Besides the original five sites, less exposed O surface sites could increase CO_2 coverage beyond 4/5 ML.

Table 2 shows the computed ΔE_{ads} for increasing CO_2 loading up to the condition of 4/5 ML.

Table 2: CO_2 adsorption energy (in eV/molecule) with increasing coverage of molecules (ML). Site is the adsorption site. $\delta\Delta E_{\text{ads}}$ informs the change of ΔE_{ads} upon the addition of a CO_2 molecule. CO_3^{2-} indicates whether the addition of a new CO_2 molecule promotes carbonate formation.

ML	Site	ΔE_{ads}	$\delta\Delta E_{\text{ads}}$	CO_3^{2-}
1/5	O[LiLaZr]	-2.21	—	Yes
2/5	O[Li2La]	-1.85	+0.36	Yes
3/5	O[LiLaZr]	-1.75	+0.10	Yes
4/5	O[LiLaZr]	-1.62	+0.13	Yes

Figure 4(a) shows structure schematics and $\Delta\Omega$ diagram for each adsorption step toward the 4/5 ML coverage. $\Delta\Omega$ is defined as in Eq. 3-4, and here it is calculated at 300 K and a CO_2 partial pressure of 1 bar.

In regimes of high-coverage, adsorption of multiple CO_2 interact with the surface in the same way as singly adsorbed CO_2 molecules, transforming into CO_3^{2-} units. At the highest calculated coverage of 4/5 ML, all adsorbed CO_2 react with the surface and form carbonates. As the coverage increases, $\Delta\Omega$ continuously decreases, indicating that the reaction between the surface and an increasing amount of CO_2 (up to 4/5 ML) is thermodynamically favorable. However, from Figure 4, one observes that absolute difference of $\Delta\Omega$ between consecutive steps decreases progressively, similar to trends of Figure 3(a). Figure 4 and Table 2 show that each oxygen species at the $\text{Li}_7\text{La}_3\text{Zr}_2\text{O}_{12}$ surface become increasingly less reactive as the CO_2 coverage increases, which contributes to a progressive decrease of the ΔE_{ads} and $\Delta\Omega$.

Figures 4(b-d) show $\Delta\Omega$ at technologically relevant temperature and CO_2 partial pressures. As the temperature increases, the adsorption and reaction of CO_2 become less favor-

able, and the preferred coverage decreases from 4/5 ML to conditions of CO₂-free surfaces. Similarly to the H₂O case, at low temperature even higher CO₂ coverage than 4/5 ML may become accessible. However, this does not change significantly the situation of low CO₂-free surfaces at high temperature, as shown in Figure 4(b-d). As the CO₂ partial pressure decreases from atmospheric to ultra-high vacuum, the formation of carbonates species at the Li₇La₃Zr₂O₁₂ surfaces appear less favorable, with the stability ranges of temperature expand accordingly. This indicates that low CO₂ partial pressures are beneficial to minimize the carbonate contamination of Li₇La₃Zr₂O₁₂ surfaces.

3.4 CO₂ and H₂O co-adsorption on Li₇La₃Zr₂O₁₂

Having previously demonstrated the pronounced reactivity of Li₇La₃Zr₂O₁₂ surface with H₂O and CO₂, we verify the possibility of H₂O and CO₂ reacting concurrently with the off-stoichiometric Li-terminated (010) cut.

We investigate the co-adsorption of H₂O and CO₂ to mimic the hydroxide-mediated carbonation proposed in Ref. 19, but here mediated explicitly by the Li₇La₃Zr₂O₁₂ surfaces. We adsorbed one H₂O molecule on the most favorable site Li[3O], and then found the most favorable site to adsorb one CO₂ molecule on the same slab, see inset in Figure 5(a). In the co-adsorption model, the most favorable CO₂ site is O[LiLaZr] as for the case of individual CO₂ adsorption (see Section 3.3).

Next, we take the individual adsorption cases of H₂O and CO₂ to represent the independent adsorption reactions (Figure 5(b)). This situation corresponds to the infinitely separated adsorption of H₂O and CO₂ molecules, with the two molecules not interacting with each other. Figure 5(a) shows ΔE_{ads} of the co-adsorption of H₂O and CO₂, while Figure 5(b) shows the ΔE_{ads} for the infinitely separated of H₂O and CO₂ molecules.

The composed ΔE_{ads} of the individual adsorptions energies of H₂O ($\Delta E_{\text{ads}} \sim -1.21$ eV) and CO₂ (~ -2.21 eV) is ~ -3.42 eV, which is more negative than the energy of co-adsorption, i.e., ~ -3.25 eV. In the co-adsorption model of Figure 5(a), the adsorbed H₂O does not easily

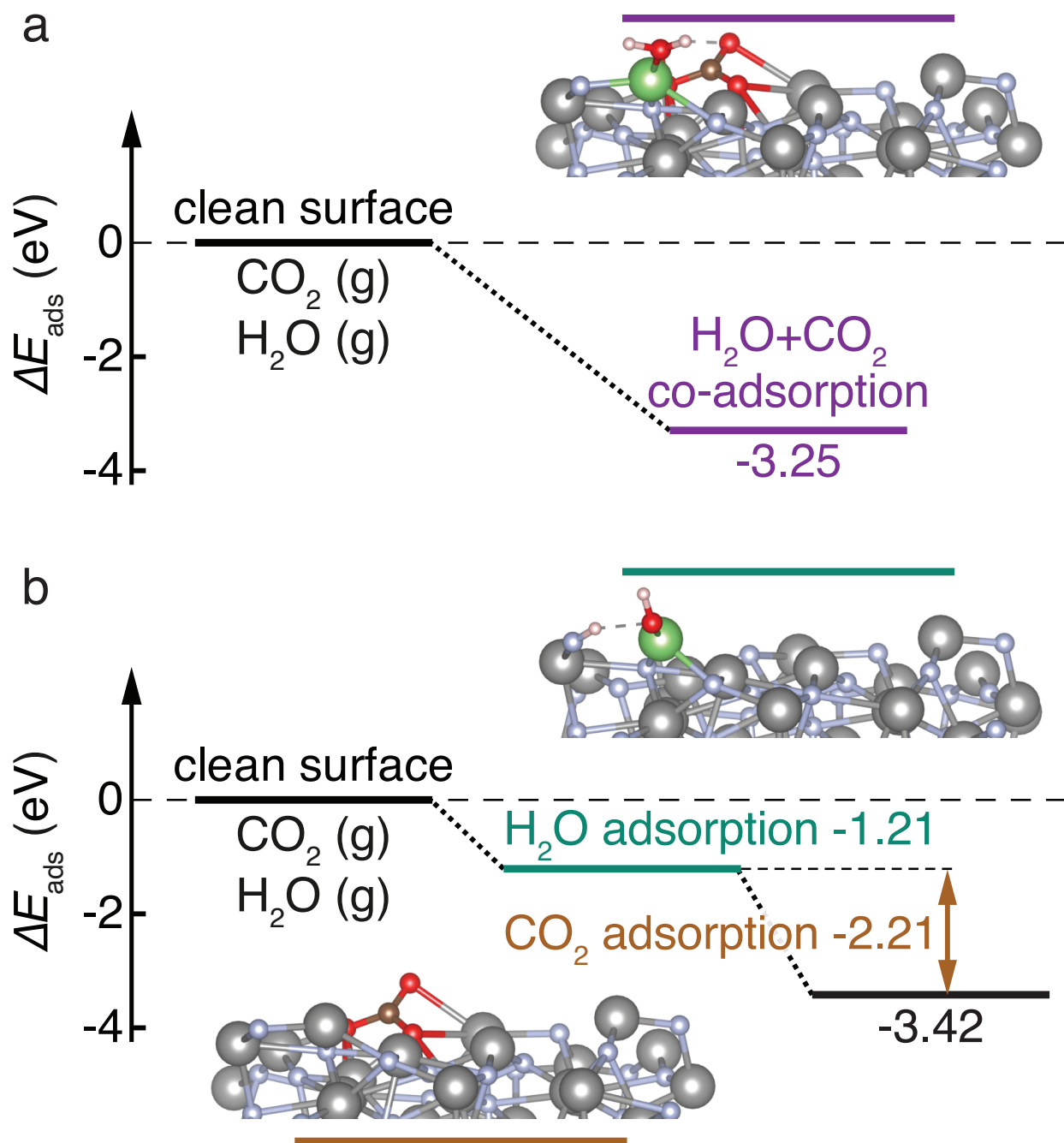


Figure 5: ΔE_{ads} for adsorption of H_2O and CO_2 : (a) co-adsorption, and (b) infinitely separated adsorption. The co-adsorption shows $\Delta E_{\text{ads}} = -3.25$ eV (in purple). The infinitely separated H_2O adsorption ($\Delta E_{\text{ads}} = -1.21$ eV, in green) and CO_2 adsorption ($\Delta E_{\text{ads}} = -2.21$ eV, in brown) show the combined adsorption energy of $\Delta E_{\text{ads}} = -3.42$ eV, more negative than the co-adsorption. The insets show schematic diagrams for adsorption structures. Atomic species not directly involved in the adsorption are greyed out.

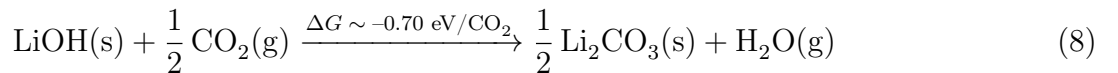
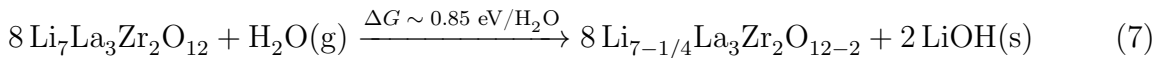
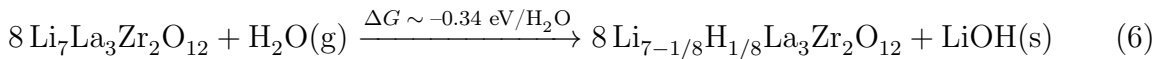
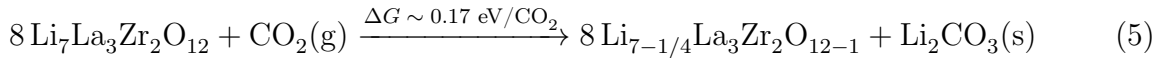
deprotonate, as opposed to the incipient H₂O dissociation (at the same site) when adsorbed individually as in Figure 5(b). These evidences clearly inform that individual reactions of H₂O and CO₂ with Li₇La₃Zr₂O₁₂ compete favorably against the concurrent co-adsorption of H₂O and CO₂. Therefore, the surface contamination of Li₇La₃Zr₂O₁₂ will be mostly driven by independent reactions of direct hydration and direct carbonation, as opposed to the hydroxide-mediated carbonation proposed in Ref. 19.

4 Discussion

Using slab calculations in the framework of *ab initio* thermodynamics, we have explored the reactivity of the complex oxide Li₇La₃Zr₂O₁₂ with two ubiquitous molecules: H₂O and CO₂. It is noted that all the adsorption processes investigated are barrier-free, which indicates fast reaction rates of H₂O and CO₂ with Li₇La₃Zr₂O₁₂. A quantitative evaluation of the reaction rates requiring microkinetic models is beyond the scope of this study.

The exposure of Li₇La₃Zr₂O₁₂ to both H₂O and CO₂ has been documented by preliminary computational and experimental studies.^{14,19,21,77}

Using X-ray photo-emission spectroscopy (XPS) depth-profiling Sharafi et al. showed the formation of Li₂CO₃ layers as thick as ~5-10 nm on the exterior of Li₇La₃Zr₂O₁₂ particles.¹⁹ From this evidence, the authors proposed several chemical reactions (Eq.s 5–8) between Li₇La₃Zr₂O₁₂, CO₂ and H₂O, whose energetics (ΔG s) were verified by first-principles calculations.¹⁹ Nevertheless, the proposed reaction mechanisms of Li₇La₃Zr₂O₁₂ carbonation are still elusive requiring in-depth investigations, which justify this endeavour.



The ΔG s in Eq.s 5–8 are from Ref. 19. In Eq. 5, Li_2CO_3 is directly formed via carbonation of $\text{Li}_7\text{La}_3\text{Zr}_2\text{O}_{12}$, but with a predicted positive ΔG .¹⁹ Compared to the unfavorable direct carbonation of $\text{Li}_7\text{La}_3\text{Zr}_2\text{O}_{12}$ (Eq. 5),¹⁹ the hydroxide-mediated carbonation was interpreted as two favorable reactions: *i*) the protonation of $\text{Li}_7\text{La}_3\text{Zr}_2\text{O}_{12}$ (Eq. 6) with H^+ exchanging with Li^+ , followed by *ii*) the conversion of LiOH and CO_2 into Li_2CO_3 as in Eq. 8. Although with unfavorable ΔG (~ 0.85 eV/ H_2O), another mechanism proposed was the direct hydration of $\text{Li}_7\text{La}_3\text{Zr}_2\text{O}_{12}$ of Eq. 7, which is followed by carbonation (of Eq. 8). Therefore, carbonate contamination on $\text{Li}_7\text{La}_3\text{Zr}_2\text{O}_{12}$ was proposed to form via the hydroxide-mediated pathway (Eq.s 6 and 8) rather than direct carbonation (Eq. 5).¹⁹

In Section 3.2 and Table 1 we have amply demonstrated the favorable adsorption of H_2O on the $\text{Li}_7\text{La}_3\text{Zr}_2\text{O}_{12}$ surfaces, with the spontaneous H_2O dissociation on exposed $\text{Li}_{\text{Surface}}$ sites as $\text{Li}_{\text{Surface}}-\text{O}-\text{H}$, thus forming LiOH species. Our calculations clearly suggest that the formation of LiOH in $\text{Li}_7\text{La}_3\text{Zr}_2\text{O}_{12}$ is mediated by its reactive surfaces, which “catalyzes” the nucleation process of lithium hydroxide moieties. Indeed, XPS of $\text{Li}_7\text{La}_3\text{Zr}_2\text{O}_{12}$ particles have detected signatures of OH^- groups, LiOH and even at relatively high temperatures (400–500 °C).²¹

Another pathway for LiOH formation proceeds through the protonation of $\text{Li}-\text{O}$ moieties exposed at the $\text{Li}_7\text{La}_3\text{Zr}_2\text{O}_{12}$ surfaces, which we also predicted as a spontaneous process. The protonation of other $\text{M}-\text{O}$ (with $\text{M} = \text{La}$ or Zr) moieties at the $\text{Li}_7\text{La}_3\text{Zr}_2\text{O}_{12}$ surfaces may also form other adventitious species, whose signatures have not been reported yet. However, the availability of free protons at the surface (resulting from readily dissociated H_2O molecules) can then be exchanged with Li^+ in $\text{Li}_7\text{La}_3\text{Zr}_2\text{O}_{12}$ as previously reported by thermo-gravimetric analysis mass-spectroscopy, neutron investigations, and as focused ion beam secondary ion mass spectrometry.^{14,77,78} Alternatively, proton species formed on the $\text{Li}_7\text{La}_3\text{Zr}_2\text{O}_{12}$ surfaces may intercalate directly into vacant Li^+ sites of the bulk structure. Note, the high Li-ion transport $\text{Li}_7\text{La}_3\text{Zr}_2\text{O}_{12}$ facilitates Li^+/H^+ exchange.

CO_3^{2-} contamination of the $\text{Li}_7\text{La}_3\text{Zr}_2\text{O}_{12}$ particle exteriors has been previously docu-

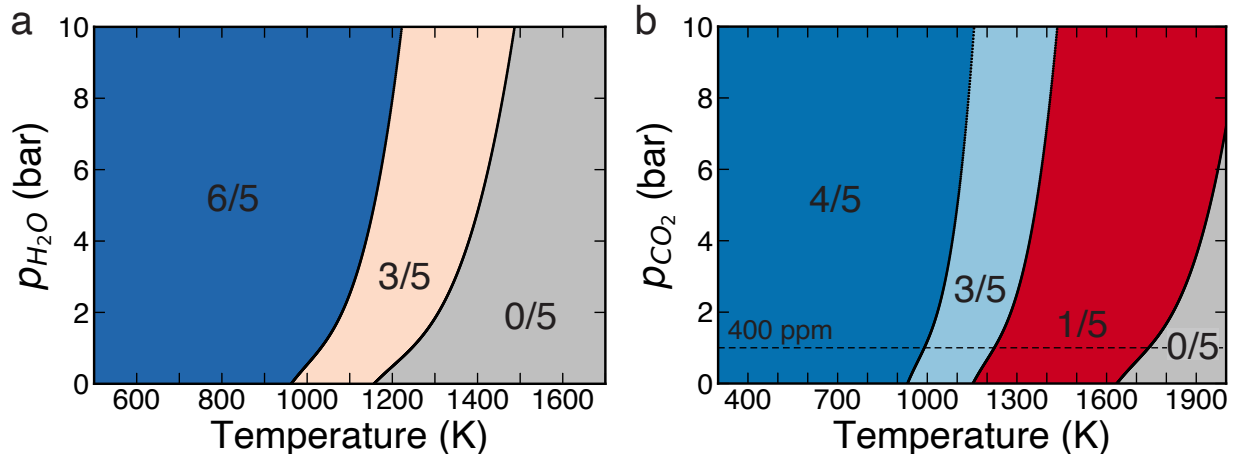


Figure 6: Surface phase diagrams of $\text{Li}_7\text{La}_3\text{Zr}_2\text{O}_{12}$ at different temperatures and partial pressures of (a) H_2O and (b) CO_2 , respectively. Fractions of monolayer (ML) and solid color denote the most favorable coverage scenarios within each range of temperature (in K) and partial pressure (in bar). The dashed line marks CO_2 level of 400 ppm at partial pressure of 1 bar. This line is used to indicate the thermodynamic favorability of adsorbing CO_2 from dilute streams, which is of relevance in CO_2 utilization.

mented through Raman and XPS measurements.^{19,21} Our calculations demonstrated spontaneous CO_2 adsorption and carbonate formation with the exposed oxygen atoms, i.e., $\text{O}_{\text{Surface}}-\text{Li}_{\text{Surface}}$ or $\text{O}_{\text{Surface}}-\text{La}_{\text{Surface}}$ (see Section 3.3 and Table 2) at the $\text{Li}_7\text{La}_3\text{Zr}_2\text{O}_{12}$ surfaces. This is in striking contrast to the unfavorable reaction of direct carbonation proposed in Eq. 5.²¹ Importantly, we show that the formation of Li_2CO_3 does not require the availability of LiOH with CO_2 , but it is directly catalyzed by the $\text{Li}_7\text{La}_3\text{Zr}_2\text{O}_{12}$ surfaces. Our surface calculations show that carbonates are not limited to Li_2CO_3 species, instead incipient CO_3^{2-} species may be bonded to other metal ions exposed at the surfaces of $\text{Li}_7\text{La}_3\text{Zr}_2\text{O}_{12}$, including Li and La. Therefore, direct carbonation of $\text{Li}_7\text{La}_3\text{Zr}_2\text{O}_{12}$ is thermodynamically favorable and barrier-free. Notably, the co-adsorption of H_2O and CO_2 appear less favorable than their individual adsorptions.

We have demonstrated the thermodynamically favorable processes of H_2O and CO_2 decomposition on the $\text{Li}_7\text{La}_3\text{Zr}_2\text{O}_{12}$ particles. We use this knowledge to prescribe external conditions (temperature and pressure) which curb the LiOH and Li_2CO_3 contamination of

$\text{Li}_7\text{La}_3\text{Zr}_2\text{O}_{12}$ during its synthesis. Figure 6 shows the computed surface phase diagrams of $\text{Li}_7\text{La}_3\text{Zr}_2\text{O}_{12}$ as functions of temperature and partial pressures of H_2O and CO_2 . The derivation of the surface phase diagrams requires the minimization of the grand-potential energy of Eq. 2 as the surface coverage, temperature, and pressures are varied.²⁴

From Figure 6, one clearly sees that scenarios of high- H_2O or CO_2 coverages are achieved at relatively high partial-pressures ($\sim 2\text{--}10$ bars) and low temperatures ($< 1,000$ K). Our predictions suggest that at atmospheric pressure (~ 1 bar) and at temperature above $\sim 1,260$ K, $\text{Li}_7\text{La}_3\text{Zr}_2\text{O}_{12}$ particles will be free of water, protons and LiOH species. More pernicious appears the carbonation of $\text{Li}_7\text{La}_3\text{Zr}_2\text{O}_{12}$, which clearly requires higher temperatures above $\sim 1,730$ K for its complete elimination at atmospheric pressures (see Figure 6(b)). These findings are representative of the real $\text{Li}_7\text{La}_3\text{Zr}_2\text{O}_{12}$ powders or the surfaces of sheet ($\text{Li}_7\text{La}_3\text{Zr}_2\text{O}_{12}$ composites), as the surface investigated dominates the $\text{Li}_7\text{La}_3\text{Zr}_2\text{O}_{12}$ Wulff shapes.^{24,79}

The synthesis of $\text{Li}_7\text{La}_3\text{Zr}_2\text{O}_{12}$ is commonly carried out via the solid-state method, by calcination in “dry” air at temperatures $\sim 1,000^\circ\text{C}$ ($\sim 1,273$ K).^{19,21,23} Procedures of densification of $\text{Li}_7\text{La}_3\text{Zr}_2\text{O}_{12}$ via hot-press (or spark-plasma) are regularly utilized to improve contact between particles and increase the electrolyte ionic conductivity. The surface phase diagrams of Figure 6, clearly show that both synthesis and sintering of $\text{Li}_7\text{La}_3\text{Zr}_2\text{O}_{12}$ should avoid air-exposure. Notably, Figure 6 informs that post-synthesis heat treatments (above $1,000^\circ\text{C}$) are beneficial to desorb H_2O and eliminate other contaminants. Indeed, typical sintering temperatures for $\text{Li}_7\text{La}_3\text{Zr}_2\text{O}_{12}$ are in the range of $1,000\text{--}1,300^\circ\text{C}$ ($\sim 1,300\text{--}1,600$ K).^{19,23} Higher temperatures than $1,300^\circ\text{C}$ may lead to significant Li (and proton) loss.²³ However, such elevated temperatures may still prevent full removal of Li_2CO_3 at the surfaces. Li loss during the $\text{Li}_7\text{La}_3\text{Zr}_2\text{O}_{12}$ preparation is typically mitigated by adding addition LiOH and Li_2CO_3 . Furthermore, we speculate that the addition of LiOH and Li_2CO_3 will not be disruptive to the preparation of $\text{Li}_7\text{La}_3\text{Zr}_2\text{O}_{12}$, and these two compounds may also limit their formation when $\text{Li}_7\text{La}_3\text{Zr}_2\text{O}_{12}$ is exposed to humid air.

Although the effect of partial pressure of H_2O and CO_2 appears less significant than

temperature with respect $\text{Li}_7\text{La}_3\text{Zr}_2\text{O}_{12}$ contamination, synthesis under ultrahigh vacuum conditions ($\sim 1 \times 10^{-6}$ bar) and at ~ 800 K guarantee water-free $\text{Li}_7\text{La}_3\text{Zr}_2\text{O}_{12}$ surfaces and sparsely contaminated by Li_2CO_3 species. Clearly, these conditions appear unpractical, but glove-box synthesis at pressures within mbars ranges (see Figures 3 and 4) may be more accessible and deserve further investigations.

Figure 6 indicates external conditions which favor (010) $\text{Li}_7\text{La}_3\text{Zr}_2\text{O}_{12}$ surfaces decorated by dissociated H_2O and carbonate species. While these surfaces may not be desired for energy storage applications, the strong adsorption of CO_2 and H_2O suggests that the off-stoichiometric (010) surface of $\text{Li}_7\text{La}_3\text{Zr}_2\text{O}_{12}$ can serve as a support in catalysis. Using two examples of water gas shift and CO_2 utilisation, we elaborate further below. Water-gas shift is typically catalyzed by noble metal nanoparticles stabilized by oxide supports. Experimental and theoretical studies have indicated that the oxide supports facilitate H_2O dissociation,^{44,45} a critical elementary step in this reaction. The favorable adsorption of H_2O and its spontaneous dissociation thus makes $\text{Li}_7\text{La}_3\text{Zr}_2\text{O}_{12}$ a promising support for the water-gas shift reaction. Indeed, there is a concerted effort to design catalytic systems which operate under dilute streams of CO_2 .^{46,47} Figure 6 illustrates that at 500-600K, 4/5 ML of CO_2 is adsorbed on $\text{Li}_7\text{La}_3\text{Zr}_2\text{O}_{12}$ even at CO_2 pressures as low as 400 ppm. Hence, the strong adsorption strength of CO_2 on $\text{Li}_7\text{La}_3\text{Zr}_2\text{O}_{12}$ makes this material a promising support for dual-functional catalysts, which adsorb CO_2 from dilute streams and further hydrogenate it to chemicals, such as methanol and ethylene over metal nanoparticles dispersed on $\text{Li}_7\text{La}_3\text{Zr}_2\text{O}_{12}$.

5 Conclusions

In summary, using a robust *ab initio* thermodynamic framework, we investigated the complex surface reactivity of $\text{Li}_7\text{La}_3\text{Zr}_2\text{O}_{12}$ toward ubiquitous H_2O and CO_2 . Li-terminated off-stoichiometric surfaces of $\text{Li}_7\text{La}_3\text{Zr}_2\text{O}_{12}$ readily react with H_2O and CO_2 , which promotes the direct formation of LiOH and Li_2CO_3 . We demonstrated that synthesis within mbar

pressure can lead to water-free $\text{Li}_7\text{La}_3\text{Zr}_2\text{O}_{12}$ surfaces and reduce drastically the amount of Li_2CO_3 formed. Our in-depth analysis provides strategies and opportunities to improve the synthesis conditions of $\text{Li}_7\text{La}_3\text{Zr}_2\text{O}_{12}$ and similar complex oxides of high technological relevance in batteries and for catalysis. The strong adsorption of CO_2 under conditions of low partial pressure and of H_2O indicates the potential of $\text{Li}_7\text{La}_3\text{Zr}_2\text{O}_{12}$ as a suitable catalyst support for the hydrogenation of dilute CO_2 streams and the water-gas shift reaction respectively. These findings are general and provide thumb rules to analyze the reactivity of complex oxides toward two common molecules, i.e., H_2O and CO_2 .

Acknowledgement

Y.L. and P.C. are grateful to the ANR-NRF NRF2019-NRF-ANR073 Na-MASTER. P.C. acknowledges funding from the National Research Foundation under his NRF Fellowship NRFF12-2020-0012. T. S. C. gratefully acknowledges funding from the Ministry of Education Academic Research Fund Tier-1 RS04/19 and RG5/21. A. M. P. acknowledges Nanyang Technological University for a Research Scholarship. The computational work was performed on resources of the National Supercomputing Centre, Singapore (<https://www.nsc.sg>).

Supporting Information Available

The supporting information includes: *i*) Benchmark tests on the effect of vdW corrections, *ii*) convergence tests of slab calculations, *iii*) structure of the slab unit cell, *iv*) tests on single-point energy cutoffs, *v*) the description of the metal sites' local environment and H_2O dissociation, *vi*) calculation results for forced H_2O dissociation at high coverage, *vii*) geometry of surface carbonates formed at the surfaces and Li_2CO_3 , and *viii*) Mulliken charges of sites post-adsorption.

References

- (1) Dunn, B.; Kamath, H.; Tarascon, J.-M. Electrical Energy Storage for the Grid: A Battery of Choices. *Science* **2011**, *334*, 928–935.
- (2) Nykvist, B.; Nilsson, M. Rapidly Falling Costs of Battery Packs for Electric Vehicles. *Nature Clim Change* **2015**, *5*, 329–332.
- (3) Cano, Z. P.; Banham, D.; Ye, S.; Hintennach, A.; Lu, J.; Fowler, M.; Chen, Z. Batteries and Fuel Cells for Emerging Electric Vehicle Markets. *Nat Energy* **2018**, *3*, 279–289.
- (4) Warburton, R. E.; Kim, J. J.; Patel, S.; Howard, J. D.; Curtiss, L. A.; Wolverton, C.; Buchholz, D. B.; Vaughey, J. T.; Fenter, P.; Fister, T. T.; Greeley, J. Tailoring Interfaces in Solid-State Batteries Using Interfacial Thermochemistry and Band Alignment. *Chem. Mater.* **2021**, *33*, 8447–8459.
- (5) Goodenough, J. B.; Kim, Y. Challenges for Rechargeable Li Batteries. *Chem. Mater.* **2010**, *22*, 587–603.
- (6) Bachman, J. C.; Muy, S.; Grimaud, A.; Chang, H.-H.; Pour, N.; Lux, S. F.; Paschos, O.; Maglia, F.; Lupart, S.; Lamp, P.; Giordano, L.; Shao-Horn, Y. Inorganic Solid-State Electrolytes for Lithium Batteries: Mechanisms and Properties Governing Ion Conduction. *Chem. Rev.* **2016**, *116*, 140–162.
- (7) Zhang, Z.; Shao, Y.; Lotsch, B.; Hu, Y.-S.; Li, H.; Janek, J.; Nazar, L. F.; Nan, C.-W.; Maier, J.; Armand, M.; Chen, L. New Horizons for Inorganic Solid State Ion Conductors. *Energy Environ. Sci.* **2018**, *11*, 1945–1976.
- (8) Janek, J.; Zeier, W. G. A Solid Future for Battery Development. *Nat Energy* **2016**, *1*, 16141.
- (9) Famprikis, T.; Canepa, P.; Dawson, J. A.; Islam, M. S.; Masquelier, C. Fundamentals of Inorganic Solid-State Electrolytes for Batteries. *Nat. Mater.* **2019**, *18*, 1278–1291.

- (10) Thangadurai, V.; Kaack, H.; Weppner, W. J. F. Novel Fast Lithium Ion Conduction in Garnet-Type $\text{Li}_{5-x}\text{La}_3\text{M}_2\text{O}_{12}$ ($\text{M} = \text{Nb}, \text{Ta}$). *Journal of the American Ceramic Society* **2003**, *86*, 437–440.
- (11) Murugan, R.; Thangadurai, V.; Weppner, W. Fast Lithium Ion Conduction in Garnet-Type $\text{Li}_7\text{La}_3\text{Zr}_2\text{O}_{12}$. *Angew. Chem. Int. Ed.* **2007**, *46*, 7778–7781.
- (12) Buschmann, H.; Dölle, J.; Berendts, S.; Kuhn, A.; Bottke, P.; Wilkening, M.; Heitjans, P.; Senyshyn, A.; Ehrenberg, H.; Lotnyk, A.; Duppel, V.; Kienle, L.; Janek, J. Structure and Dynamics of the Fast Lithium Ion Conductor “ $\text{Li}_7\text{La}_3\text{Zr}_2\text{O}_{12}$ ”. *Phys. Chem. Chem. Phys.* **2011**, *13*, 19378.
- (13) Toda, S.; Ishiguro, K.; Shimonishi, Y.; Hirano, A.; Takeda, Y.; Yamamoto, O.; Imanishi, N. Low Temperature Cubic Garnet-Type CO_2 -Doped $\text{Li}_7\text{La}_3\text{Zr}_2\text{O}_{12}$. *Solid State Ionics* **2013**, *233*, 102–106.
- (14) Galven, C.; Dittmer, J.; Suard, E.; Le Berre, F.; Crosnier-Lopez, M.-P. Instability of Lithium Garnets against Moisture. Structural Characterization and Dynamics of $\text{Li}_{7-x}\text{H}_x\text{La}_3\text{Sn}_2\text{O}_{12}$ and $\text{Li}_{5-x}\text{H}_x\text{La}_3\text{Nb}_2\text{O}_{12}$. *Chem. Mater.* **2012**, *24*, 3335–3345.
- (15) Allen, J.; Wolfenstine, J.; Rangasamy, E.; Sakamoto, J. Effect of Substitution (Ta, Al, Ga) on the Conductivity of $\text{Li}_7\text{La}_3\text{Zr}_2\text{O}_{12}$. *Journal of Power Sources* **2012**, *206*, 315–319.
- (16) Thangadurai, V.; Narayanan, S.; Pinzaru, D. Garnet-Type Solid-State Fast Li Ion Conductors for Li Batteries: Critical Review. *Chem. Soc. Rev.* **2014**, *43*, 4714.
- (17) Mukhopadhyay, S.; Thompson, T.; Sakamoto, J.; Huq, A.; Wolfenstine, J.; Allen, J. L.; Bernstein, N.; Stewart, D. A.; Johannes, M. D. Structure and Stoichiometry in Super-valent Doped $\text{Li}_7\text{La}_3\text{Zr}_2\text{O}_{12}$. *Chem. Mater.* **2015**, *27*, 3658–3665.

- (18) Cheng, L.; Wu, C. H.; Jarry, A.; Chen, W.; Ye, Y.; Zhu, J.; Kostecki, R.; Persson, K.; Guo, J.; Salmeron, M.; Chen, G.; Doeff, M. Interrelationships among Grain Size, Surface Composition, Air Stability, and Interfacial Resistance of Al-Substituted $\text{Li}_7\text{La}_3\text{Zr}_2\text{O}_{12}$ Solid Electrolytes. *ACS Appl. Mater. Interfaces* **2015**, *7*, 17649–17655.
- (19) Sharafi, A.; Yu, S.; Naguib, M.; Lee, M.; Ma, C.; Meyer, H. M.; Nanda, J.; Chi, M.; Siegel, D. J.; Sakamoto, J. Impact of Air Exposure and Surface Chemistry on Li– $\text{Li}_7\text{La}_3\text{Zr}_2\text{O}_{12}$ Interfacial Resistance. *J. Mater. Chem. A* **2017**, *5*, 13475–13487.
- (20) Porz, L.; Swamy, T.; Sheldon, B. W.; Rettenwander, D.; Frömling, T.; Thaman, H. L.; Berendts, S.; Uecker, R.; Carter, W. C.; Chiang, Y.-M. Mechanism of Lithium Metal Penetration through Inorganic Solid Electrolytes. *Adv. Energy Mater.* **2017**, *7*, 1701003.
- (21) Sharafi, A.; Kazyak, E.; Davis, A. L.; Yu, S.; Thompson, T.; Siegel, D. J.; Dasgupta, N. P.; Sakamoto, J. Surface Chemistry Mechanism of Ultra-Low Interfacial Resistance in the Solid-State Electrolyte $\text{Li}_7\text{La}_3\text{Zr}_2\text{O}_{12}$. *Chem. Mater.* **2017**, *29*, 7961–7968.
- (22) Han, X.; Gong, Y.; Fu, K. K.; He, X.; Hitz, G. T.; Dai, J.; Pearse, A.; Liu, B.; Wang, H.; Rubloff, G.; Mo, Y.; Thangadurai, V.; Wachsman, E. D.; Hu, L. Negating Interfacial Impedance in Garnet-Based Solid-State Li Metal Batteries. *Nature Mater* **2017**, *16*, 572–579.
- (23) Sharafi, A.; Haslam, C. G.; Kerns, R. D.; Wolfenstine, J.; Sakamoto, J. Controlling and Correlating the Effect of Grain Size with the Mechanical and Electrochemical Properties of $\text{Li}_7\text{La}_3\text{Zr}_2\text{O}_{12}$ Solid-State Electrolyte. *J. Mater. Chem. A* **2017**, *5*, 21491–21504.
- (24) Canepa, P.; Dawson, J. A.; Sai Gautam, G.; Statham, J. M.; Parker, S. C.; Islam, M. S. Particle Morphology and Lithium Segregation to Surfaces of the $\text{Li}_7\text{La}_3\text{Zr}_2\text{O}_{12}$ Solid Electrolyte. *Chem. Mater.* **2018**, *30*, 3019–3027.

- (25) Kasemchainan, J.; Zekoll, S.; Spencer Jolly, D.; Ning, Z.; Hartley, G. O.; Marrow, J.; Bruce, P. G. Critical Stripping Current Leads to Dendrite Formation on Plating in Lithium Anode Solid Electrolyte Cells. *Nat. Mater.* **2019**, *18*, 1105–1111.
- (26) Annamalai, L.; Liu, Y.; Ezenwa, S.; Dang, Y.; Suib, S. L.; Deshlahra, P. Influence of Tight Confinement on Selective Oxidative Dehydrogenation of Ethane on MoVTaNb Mixed Oxides. *ACS Catal.* **2018**, *8*, 7051–7067.
- (27) Licht, R. B.; Bell, A. T. A DFT Investigation of the Mechanism of Propene Ammoxidation over α -Bismuth Molybdate. *ACS Catal.* **2017**, *7*, 161–176.
- (28) Brookes, C.; Wells, P. P.; Cibir, G.; Dimitratos, N.; Jones, W.; Morgan, D. J.; Bowker, M. Molybdenum Oxide on Fe₂O₃ Core–Shell Catalysts: Probing the Nature of the Structural Motifs Responsible for Methanol Oxidation Catalysis. *ACS Catal.* **2014**, *4*, 243–250.
- (29) Li, X.; Teschner, D.; Streibel, V.; Lunkenbein, T.; Masliuk, L.; Fu, T.; Wang, Y.; Jones, T.; Seitz, F.; Girgsdies, F.; Rosowski, F.; Schlögl, R.; Trunschke, A. How to Control Selectivity in Alkane Oxidation? *Chem. Sci.* **2019**, *10*, 2429–2443.
- (30) Trunschke, A.; Noack, J.; Trojanov, S.; Girgsdies, F.; Lunkenbein, T.; Pfeifer, V.; Hävecker, M.; Kube, P.; Sprung, C.; Rosowski, F.; Schlögl, R. The Impact of the Bulk Structure on Surface Dynamics of Complex Mo–V-Based Oxide Catalysts. *ACS Catal.* **2017**, *7*, 3061–3071.
- (31) Li, Y.; Fu, Q.; Flytzani-Stephanopoulos, M. Low-Temperature Water-Gas Shift Reaction over Cu- and Ni-Loaded Cerium Oxide Catalysts. *Applied Catalysis B: Environmental* **2000**, *27*, 179–191.
- (32) Tanaka, Y. Water Gas Shift Reaction for the Reformed Fuels over Cu/MnO Catalysts Prepared via Spinel-Type Oxide. *Journal of Catalysis* **2003**, *215*, 271–278.

- (33) Papavasiliou, J.; Avgouropoulos, G.; Ioannides, T. Combined Steam Reforming of Methanol over Cu–Mn Spinel Oxide Catalysts. *Journal of Catalysis* **2007**, *251*, 7–20.
- (34) Rodriguez, J. A.; Ma, S.; Liu, P.; Hrbek, J.; Evans, J.; Pérez, M. Activity of CeO_x and TiO_x Nanoparticles Grown on Au(111) in the Water-Gas Shift Reaction. *Science* **2007**, *318*, 1757–1760.
- (35) Rodriguez, J.; Liu, P.; Wang, X.; Wen, W.; Hanson, J.; Hrbek, J.; Pérez, M.; Evans, J. Water-Gas Shift Activity of Cu Surfaces and Cu Nanoparticles Supported on Metal Oxides. *Catalysis Today* **2009**, *143*, 45–50.
- (36) McFarland, E. W.; Metiu, H. Catalysis by Doped Oxides. *Chem. Rev.* **2013**, *113*, 4391–4427.
- (37) Nelson, N. C.; Nguyen, M.-T.; Glezakou, V.-A.; Rousseau, R.; Szanyi, J. Carboxyl Intermediate Formation via an in Situ-Generated Metastable Active Site during Water-Gas Shift Catalysis. *Nat Catal* **2019**, *2*, 916–924.
- (38) Wang, S.; Lu, G. Q. M.; Millar, G. J. Carbon Dioxide Reforming of Methane To Produce Synthesis Gas over Metal-Supported Catalysts: State of the Art. *Energy Fuels* **1996**, *10*, 896–904.
- (39) Muroyama, H.; Tsuda, Y.; Asakoshi, T.; Masitah, H.; Okanishi, T.; Matsui, T.; Eguchi, K. Carbon Dioxide Methanation over Ni Catalysts Supported on Various Metal Oxides. *Journal of Catalysis* **2016**, *343*, 178–184.
- (40) Yang, E.-h.; Noh, Y. S.; Hong, G. H.; Moon, D. J. Combined Steam and CO₂ Reforming of Methane over La_{1-x}Sr_xNiO₃ Perovskite Oxides. *Catalysis Today* **2018**, *299*, 242–250.
- (41) Derk, A. R.; Moore, G. M.; Sharma, S.; McFarland, E. W.; Metiu, H. Catalytic Dry Reforming of Methane on Ruthenium-Doped Ceria and Ruthenium Supported on Ceria. *Top Catal* **2014**, *57*, 118–124.

- (42) Wang, J.; Li, G.; Li, Z.; Tang, C.; Feng, Z.; An, H.; Liu, H.; Liu, T.; Li, C. A Highly Selective and Stable ZnO-ZrO₂ Solid Solution Catalyst for CO₂ Hydrogenation to Methanol. *Sci. Adv.* **2017**, *3*, e1701290.
- (43) Huš, M.; Kopač, D.; Likozar, B. Catalytic Hydrogenation of Carbon Dioxide to Methanol: Synergistic Effect of Bifunctional Cu/Perovskite Catalysts. *ACS Catal.* **2019**, *9*, 105–116.
- (44) Zhao, Z.-J.; Li, Z.; Cui, Y.; Zhu, H.; Schneider, W. F.; Delgass, W. N.; Ribeiro, F.; Greeley, J. Importance of Metal-Oxide Interfaces in Heterogeneous Catalysis: A Combined DFT, Microkinetic, and Experimental Study of Water-Gas Shift on Au/MgO. *Journal of Catalysis* **2017**, *345*, 157–169.
- (45) Nelson, N. C.; Szanyi, J. Heterolytic Hydrogen Activation: Understanding Support Effects in Water–Gas Shift, Hydrodeoxygenation, and CO Oxidation Catalysis. *ACS Catal.* **2020**, *10*, 5663–5671.
- (46) Sen, R.; Goeppert, A.; Kar, S.; Prakash, G. K. S. Hydroxide Based Integrated CO₂ Capture from Air and Conversion to Methanol. *J. Am. Chem. Soc.* **2020**, *142*, 4544–4549.
- (47) Omodolor, I. S.; Otor, H. O.; Andonegui, J. A.; Allen, B. J.; Alba-Rubio, A. C. Dual-Function Materials for CO₂ Capture and Conversion: A Review. *Ind. Eng. Chem. Res.* **2020**, *59*, 17612–17631.
- (48) Kohn, W.; Sham, L. J. Self-Consistent Equations Including Exchange and Correlation Effects. *Phys. Rev.* **1965**, *140*, A1133–A1138.
- (49) Perdew, J. P.; Burke, K.; Ernzerhof, M. Generalized Gradient Approximation Made Simple. *Phys. Rev. Lett.* **1996**, *77*, 3865–3868.

- (50) Grimme, S.; Antony, J.; Ehrlich, S.; Krieg, H. A Consistent and Accurate *Ab Initio* Parametrization of Density Functional Dispersion Correction (DFT-D) for the 94 Elements H-Pu. *The Journal of Chemical Physics* **2010**, *132*, 154104.
- (51) Grimme, S.; Ehrlich, S.; Goerigk, L. Effect of the Damping Function in Dispersion Corrected Density Functional Theory. *J. Comput. Chem.* **2011**, *32*, 1456–1465.
- (52) Becke, A. D.; Johnson, E. R. Exchange-Hole Dipole Moment and the Dispersion Interaction Revisited. *The Journal of Chemical Physics* **2007**, *127*, 154108.
- (53) Kresse, G.; Furthmüller, J. Efficiency of Ab-Initio Total Energy Calculations for Metals and Semiconductors Using a Plane-Wave Basis Set. *Computational Materials Science* **1996**, *6*, 15–50.
- (54) Kresse, G.; Furthmüller, J. Efficient Iterative Schemes for *Ab Initio* Total-Energy Calculations Using a Plane-Wave Basis Set. *Phys. Rev. B* **1996**, *54*, 11169–11186.
- (55) Kresse, G.; Hafner, J. *Ab Initio* Molecular Dynamics for Liquid Metals. *Phys. Rev. B* **1993**, *47*, 558–561.
- (56) Kresse, G.; Joubert, D. From Ultrasoft Pseudopotentials to the Projector Augmented-Wave Method. *Phys. Rev. B* **1999**, *59*, 1758–1775.
- (57) Choksi, T. S.; Roling, L. T.; Streibel, V.; Abild-Pedersen, F. Predicting Adsorption Properties of Catalytic Descriptors on Bimetallic Nanoalloys with Site-Specific Precision. *J. Phys. Chem. Lett.* **2019**, *10*, 1852–1859.
- (58) Maintz, S.; Deringer, V. L.; Tchougréeff, A. L.; Dronskowski, R. LOBSTER: A Tool to Extract Chemical Bonding from Plane-Wave Based DFT: Tool to Extract Chemical Bonding. *J. Comput. Chem.* **2016**, *37*, 1030–1035.
- (59) Butler, K. T.; Sai Gautam, G.; Canepa, P. Designing Interfaces in Energy Materials Applications with First-Principles Calculations. *npj Comput Mater* **2019**, *5*, 19.

- (60) Chase, M. W., National Institute of Standards and Technology (U.S.), Eds. *NIST-JANAF Thermochemical Tables*, 4th ed.; American Chemical Society ; American Institute of Physics for the National Institute of Standards and Technology: Washington, DC : New York, 1998; Issued as: Journal of physical and chemical reference data; monograph no. 9, 1998.
- (61) Ong, S. P.; Richards, W. D.; Jain, A.; Hautier, G.; Kocher, M.; Cholia, S.; Gunter, D.; Chevrier, V. L.; Persson, K. A.; Ceder, G. Python Materials Genomics (Pymatgen): A Robust, Open-Source Python Library for Materials Analysis. *Computational Materials Science* **2013**, *68*, 314–319.
- (62) Tasker, P. W. The Stability of Ionic Crystal Surfaces. *J. Phys. C: Solid State Phys.* **1979**, *12*, 4977–4984.
- (63) Szabo, A.; Ostlund, N. S. *Modern Quantum Chemistry: Introduction to Advanced Electronic Structure Theory*; Dover Publications: Mineola, N.Y, 1996; Previously published: 1st ed., rev. New York : McGraw-Hill, c1989.
- (64) Parr, R. G.; Pearson, R. G. Absolute Hardness: Companion Parameter to Absolute Electronegativity. *J. Am. Chem. Soc.* **1983**, *105*, 7512–7516.
- (65) Dronskowski, R. *Computational Chemistry of Solid State Materials: A Guide for Materials Scientists, Chemists, Physicists and Others*, 1st ed.; Wiley, 2005.
- (66) Wang, Z.-T.; Wang, Y.-G.; Mu, R.; Yoon, Y.; Dahal, A.; Schenter, G. K.; Glezakou, V.-A.; Rousseau, R.; Lyubinetsky, I.; Dohnálek, Z. Probing Equilibrium of Molecular and Deprotonated Water on TiO_2 (110). *Proc Natl Acad Sci USA* **2017**, *114*, 1801–1805.
- (67) Calegari Andrade, M. F.; Ko, H.-Y.; Zhang, L.; Car, R.; Selloni, A. Free Energy of Proton Transfer at the Water– TiO_2 Interface from *Ab Initio* Deep Potential Molecular Dynamics. *Chem. Sci.* **2020**, *11*, 2335–2341.

- (68) Nguyen, M.-T.; Mu, R.; Cantu, D. C.; Lyubinetsky, I.; Glezakou, V.-A.; Dohnálek, Z.; Rousseau, R. Dynamics, Stability, and Adsorption States of Water on Oxidized RuO₂ (110). *J. Phys. Chem. C* **2017**, *121*, 18505–18515.
- (69) Choksi, T.; Greeley, J. Partial Oxidation of Methanol on MoO₃ (010): A DFT and Microkinetic Study. *ACS Catal.* **2016**, *6*, 7260–7277.
- (70) Metiu, H.; Chrétien, S.; Hu, Z.; Li, B.; Sun, X. Chemistry of Lewis Acid–Base Pairs on Oxide Surfaces. *J. Phys. Chem. C* **2012**, *116*, 10439–10450.
- (71) Kakekhani, A.; Roling, L. T.; Kulkarni, A.; Latimer, A. A.; Abroshan, H.; Schumann, J.; AlJama, H.; Siahrostami, S.; Ismail-Beigi, S.; Abild-Pedersen, F.; Nørskov, J. K. Nature of Lone-Pair–Surface Bonds and Their Scaling Relations. *Inorg. Chem.* **2018**, *57*, 7222–7238.
- (72) Mu, R.; Cantu, D. C.; Lin, X.; Glezakou, V.-A.; Wang, Z.; Lyubinetsky, I.; Rousseau, R.; Dohnálek, Z. Dimerization Induced Deprotonation of Water on RuO₂ (110). *J. Phys. Chem. Lett.* **2014**, *5*, 3445–3450.
- (73) Mu, R.; Cantu, D. C.; Glezakou, V.-A.; Lyubinetsky, I.; Rousseau, R.; Dohnálek, Z. Deprotonated Water Dimers: The Building Blocks of Segmented Water Chains on Rutile RuO₂ (110). *J. Phys. Chem. C* **2015**, *119*, 23552–23558.
- (74) Nadeem, I. M.; Treacy, J. P. W.; Selcuk, S.; Torrelles, X.; Hussain, H.; Wilson, A.; Grinter, D. C.; Cabailh, G.; Bikondoa, O.; Nicklin, C.; Selloni, A.; Zegenhagen, J.; Lindsay, R.; Thornton, G. Water Dissociates at the Aqueous Interface with Reduced Anatase TiO₂ (101). *J. Phys. Chem. Lett.* **2018**, *9*, 3131–3136.
- (75) Tsuji, H.; Okamura-Yoshida, A.; Shishido, T.; Hattori, H. Dynamic Behavior of Carbonate Species on Metal Oxide Surface: Oxygen Scrambling between Adsorbed Carbon Dioxide and Oxide Surface. *Langmuir* **2003**, *19*, 8793–8800.

- (76) Idemoto, Y.; Richardson, J. W.; Koura, N.; Kohara, S.; Loong, C.-K. Crystal Structure of $(\text{Li}_x\text{K}_{1-x})_2\text{CO}_3$ ($x = 0, 0.43, 0.5, 0.62, 1$) by Neutron Powder Diffraction Analysis. *Journal of Physics and Chemistry of Solids* **1998**, *59*, 363–376.
- (77) Larraz, G.; Orera, A.; Sanjuán, M. L. Cubic Phases of Garnet-Type $\text{Li}_7\text{La}_3\text{Zr}_2\text{O}_{12}$: The Role of Hydration. *J. Mater. Chem. A* **2013**, *1*, 11419.
- (78) Brugge, R. H.; Hekselman, A. K. O.; Cavallaro, A.; Pesci, F. M.; Chater, R. J.; Kilner, J. A.; Aguadero, A. Garnet Electrolytes for Solid State Batteries: Visualization of Moisture-Induced Chemical Degradation and Revealing Its Impact on the Li-Ion Dynamics. *Chem. Mater.* **2018**, *30*, 3704–3713.
- (79) Awaka, J.; Kijima, N.; Hayakawa, H.; Akimoto, J. Synthesis and Structure Analysis of Tetragonal $\text{Li}_7\text{La}_3\text{Zr}_2\text{O}_{12}$ with the Garnet-Related Type Structure. *Journal of Solid State Chemistry* **2009**, *182*, 2046–2052.